

Estimating the dust production rate of carbon stars in the Small Magellanic Cloud

Ambra Nanni,^{1*} Paola Marigo,¹ Léo Girardi,² Stefano Rubele,¹ Alessandro Bressan,³ Martin A. T. Groenewegen,⁴ Giada Pastorelli¹ and Bernhard Aringer¹

¹Dipartimento di Fisica e Astronomia Galileo Galilei, Università di Padova, Vicolo dell'Osservatorio 3, I-35122 Padova, Italy

²Osservatorio Astronomico di Padova, Vicolo dell'Osservatorio 5, I-35122 Padova, Italy

³SISSA, via Bonomea 265, I-34136 Trieste, Italy

⁴Koninklijke Sterrenwacht van België, Ringlaan 3, B-1180 Brussel, Belgium

Accepted 2017 October 6. Received 2017 October 4; in original form 2017 July 28

ABSTRACT

We employ newly computed grids of spectra reprocessed by dust for estimating the total dust production rate (DPR) of carbon stars in the Small Magellanic Cloud (SMC). For the first time, the grids of spectra are computed as a function of the main stellar parameters, i.e. mass-loss rate, luminosity, effective temperature, current stellar mass and element abundances at the photosphere, following a consistent, physically grounded scheme of dust growth coupled with stationary wind outflow. The model accounts for the dust growth of various dust species formed in the circumstellar envelopes of carbon stars, such as carbon dust, silicon carbide and metallic iron. In particular, we employ some selected combinations of optical constants and grain sizes for carbon dust that have been shown to reproduce simultaneously the most relevant colour–colour diagrams in the SMC. By employing our grids of models, we fit the spectral energy distributions of ≈ 3100 carbon stars in the SMC, consistently deriving some important dust and stellar properties, i.e. luminosities, mass-loss rates, gas-to-dust ratios, expansion velocities and dust chemistry. We discuss these properties and we compare some of them with observations in the Galaxy and Large Magellanic Cloud. We compute the DPR of carbon stars in the SMC, finding that the estimates provided by our method can be significantly different, between a factor of ≈ 2 – 5 , than the ones available in the literature. Our grids of models, including the spectra and other relevant dust and stellar quantities, are publicly available at <http://starkey.astro.unipd.it/web/guest/dustymodels>.

Key words: stars: AGB and post-AGB – stars: carbon – circumstellar matter – stars: mass-loss – stars: winds, outflows – Magellanic Clouds.

1 INTRODUCTION

Carbon (C)-rich stars on the thermally pulsing asymptotic giant branch (TP-AGB) are characterized by luminous and cool atmospheres with plenty of spectral features from C-bearing molecules, and by extended dust-rich circumstellar envelopes (CSEs). Dust grains can deeply modify the emerging spectral energy distributions (SEDs) of such stars, because they absorb the photospheric stellar radiation and re-emit it at longer wavelength. In addition to that, photons are also scattered by dust grains. As a consequence, C-rich stars are extremely relevant for the interpretation of the near- and mid-infrared (NIR and MIR) colours of both resolved and unresolved stellar populations. This is especially true at the lower-than-

solar metallicities that characterize most dwarf galaxies, for which a large fraction of the TP-AGB stars evolve through a C-rich phase.

Indeed, galaxies such as the Magellanic Clouds contain rich population of C stars that can be classified roughly in three groups: (1) those belonging to the ‘red tail’ of C stars, with $J - K_s$ colours between 1.2 and ≈ 2 mag (Cioni et al. 2006); (2) the dust-obscured sources classified as ‘extreme AGB stars’ (X-stars), extending to much redder $J - K_s$ colours, which are most likely to be C-rich (van Loon et al. 1997, 2006, 2008; Matsuura et al. 2009) and finally (3) C-rich members among the class dubbed ‘anomalous O-rich AGB stars’ (hereafter aAGB stars) by Boyer et al. (2011), which have $J - K_s$ similar to those of O-rich stars but redder $J - [8]$ colours. Their infrared (IR) SEDs can be derived, for a wide range of wavelengths, from high-quality photometric surveys such as the Two Micron All Sky Survey (2MASS; Skrutskie et al. 2006), and the *Spitzer* Survey of the Large Magellanic Cloud (SAGE;

* E-mail: ambra.nanni@unipd.it

Blum et al. 2006) and *Spitzer* Survey of the Small Magellanic Cloud (S³MC; Bolatto et al. 2007). As far as the Small Magellanic Cloud (SMC) is concerned, the most comprehensive set of IR data in the range between 3.6 and 160 μm is presented in the *Spitzer Space Telescope* Legacy Program ‘Surveying the Agents of Galaxy Evolution in the Tidally Stripped, Low Metallicity SMC’ (SAGE-SMC; Gordon et al. 2011), from which about 5800 TP-AGB stars have been classified (Boyer et al. 2011, 2015). A revised version of the original catalogue by Boyer et al. (2011) is presented in the TP-AGB candidate list by Srinivasan et al. (2016).

In the latest years, different groups aimed at estimating the total dust production rate (DPR) and the individual mass-loss rates of AGB stars in the Magellanic Clouds employing the SED fitting technique (van Loon 2006; Groenewegen et al. 2007, 2009; Srinivasan, Sargent & Meixner 2011; Boyer et al. 2012; Gullieuszik et al. 2012; Riebel et al. 2012; Matsuura, Woods & Owen 2013; Srinivasan et al. 2016; Goldman et al. 2017). Pre-computed grids of spectra for dusty AGB stars, employed for the SED fitting procedure, are available in the literature (Groenewegen 2006; Srinivasan et al. 2011). In the standard approach adopted in the literature, the SEDs of AGB stars are fitted by choosing a priori a given optical data set and a certain grain size or grain size distribution. However, the typical grain size of carbon dust is uncertain and several optical data sets for carbon dust, very different from each other, are available in the literature (Hanner 1988; Rouleau & Martin 1991; Zubko et al. 1996; Jager, Mutschke & Henning 1998). As discussed in Nanni et al. (2016) both the optical data set and grain size heavily affect the emerging spectra of dust-enshrouded C-rich stars and the carbon dust optical constants need to be constrained by reproducing most of the NIR and MIR colour–colour diagrams (CCDs) simultaneously. In the context of hydrodynamical models, optical constants and grain sizes of carbon dust have been also discussed by Andersen, Loidl & Höfner (1999). In addition to that, the SED fitting technique relies on assumptions related to dust chemistry, gas-to-dust ratio (usually assumed to be fixed), outflow expansion velocity, dust condensation temperature and shell geometry. The evaluation of the dust mass-loss rate is also sensitive to the dust temperature at the boundary of the inner shell, which is usually fixed, and to the typical size of dust grains, which also needs to be assumed.

In this work, we present a new grid of dusty models based on a physically grounded scheme for dust growth, coupled with a stationary wind (Nanni et al. 2013, 2014). By using such a grid of models, we fit the SEDs for all the carbon stars in the catalogue of the SMC by Srinivasan et al. (2016), and we compute their total DPR. In contrast to the standard approach used so far in the literature, our dust model consistently computes the gas-to-dust ratio, dust chemistry and outflow expansion velocity, without the need of relying on assumptions or scaling relations for these quantities. We also investigate the variations on the final dust budget produced by employing different optical data sets and grain sizes for the SED fitting. Such combinations are the ones that reproduce the most important NIR and MIR colours simultaneously in the SMC and have been selected in Nanni et al. (2016).

2 MODEL AND SED FITTING METHOD

In this section we recall the basic equations of our dust growth model and discuss the sample of carbon-rich stars fitted and the SED fitting method.

Table 1. Combination of optical data sets and seed particle abundances selected for the SED fitting.

Optical data set	$\rho_{\text{d,amC}}$ (g cm^{-3})	$\log(\epsilon_s)$	Denomination
Rouleau & Martin (1991)	1.85	−12	R12
Rouleau & Martin (1991)	1.85	−13	R13
Jager et al. (1998) ($T = 400^\circ\text{C}$)	1.435	−12	J400
Jager et al. (1998) ($T = 1000^\circ\text{C}$)	1.988	−12	J1000
Hanner (1988)	1.85	−11	H11
Zubko et al. (1996) (ACAR sample)	1.87	−12	Z12

2.1 Dust growth scheme

We adopt the dust growth scheme described in Nanni et al. (2013, 2014) that is an improved version of the description by Ferrarotti & Gail (2006) also employed, in its original formulation, by other groups (Ventura et al. 2012, 2014, 2016; Dell’Agli et al. 2015a,b). Our code requires as input quantities the stellar parameters (luminosity, L , effective temperature, T_{eff} , photospheric spectrum, actual stellar mass, M , element abundances in the atmosphere and mass-loss rate, \dot{M}), plus the seed particle abundance in the CSEs, the optical data set of the dust species and the initial conditions, which are the initial grain size $a_0 = 10^{-3} \mu\text{m}$, which is assumed to be the same for all the dust species and the initial outflow velocity $v_i = 4 \text{ km s}^{-1}$. In case the outflow is not accelerated, the dust production is computed assuming a constant value of the velocity $v_{\text{exp}} = v_i$. The value of the initial velocity is selected in order to reproduce the observed C- and X-stars in stellar population synthesis models (Pastorelli et al., in preparation).

We include as dust species amorphous carbon (amC), silicon carbide (SiC) and metallic iron. For amC we select the combinations of optical data sets and grain sizes that well reproduce several of the observed colour–colour diagrams in the NIR and MIR bands, based on Nanni et al. (2016). Such combinations are listed in Table 1. The optical data sets for SiC and metallic iron are taken from Pegourie (1988) and Leksina & Penkina (1967), respectively.

The seed abundance is assumed to be proportional to the carbon excess $\epsilon_C - \epsilon_O$:

$$\epsilon_{\text{s,C}} \propto \epsilon_s(\epsilon_C - \epsilon_O), \quad (1)$$

where ϵ_s is a free model parameter (Nanni et al. 2016). The quantities ϵ_C and ϵ_O are the number densities of carbon and oxygen atoms in the stellar atmosphere normalized by the number of hydrogen nuclei. The quantity $\epsilon_{\text{s,C}}$ is assumed to be the same for all the dust species formed.

Given the input quantities, the code integrates a set of differential equations describing the dust growth of various dust species, the stationary, spherically symmetric, outflow and the envelope structure.

For any combination of the stellar quantities, our dust scheme provides as output the outflow structure in terms of density profile, outflow velocity, dust condensation radius and dust properties, such as the chemical composition, the gas-to-dust ratio and the dust temperature at the boundary of the inner shell.

The photospheric spectra, taken from Aringer et al. (2016), are reprocessed by dust. The radiative transfer calculation is performed by means of the code More of DUSTY (MoD; Groenewegen 2012), based on DUSTY (Ivezic & Elitzur 1997). Some of the quantities computed by our dust formation code, as the optical depth at a given fiducial wavelength, τ_λ , the average optical properties consistently computed for the chemistry and grain size of the different dust

species and the dust temperature at the inner boundary of the shell, are taken as input in MoD.

We briefly recall in the following the most useful equations describing the dust growth process in CSEs (Nanni et al. 2013, 2014).

For the dust growth calculation along the CSE, the basic equations are the following.

(i) Gas temperature profile:

$$T_{\text{gas}}(r)^4 = T_{\text{eff}}^4 \left[W(r) + \frac{3}{4} \tau_L \right], \quad (2)$$

where $W(r)$ is the dilution term,

$$W(r) = \frac{1}{2} \left[1 - \sqrt{1 - \left(\frac{R_*}{r} \right)^2} \right], \quad (3)$$

and τ_L is defined by the differential equation,

$$\frac{d\tau_L}{dr} = -\rho\kappa \left(\frac{R_*}{r} \right)^2, \quad (4)$$

where κ is the average opacity of the medium computed as fully described in Nanni et al. (2013, 2014), R_* is the stellar radius, r is the distance from the centre of the star and the quantity τ_L has to be zero at infinity. Note that the temperature structure determined by equation (2) is dependent on the amount of dust produced through the term τ_L , which contains the quantity κ .

(ii) Growth rate of the dust grain radius.

Once the seed particle abundance is assumed, the grain growth proceeds through the addition of molecules on the grain surface. The differential equation that describes such a process is

$$\frac{da_i}{dt} = V_{0,i} (J_i^{\text{gr}} - J_i^{\text{dec}}), \quad (5)$$

where J_i^{gr} and J_i^{dec} are the growth and decomposition rates, respectively, and $V_{0,i}$ is the volume of one monomer of dust. The term J_i^{gr} is provided by the rate of effective collisions of the molecules impinging on the grain surface, while J_i^{dec} can be provided by pure sublimation of the dust grains due to heating from the stellar radiation and/or by the inverse reaction between H_2 molecules at the grain surface (chemisputtering).

For carbon dust the chemisputtering term is assumed to be negligible following the scheme by Cherchneff, Barker & Tielens (1992) in which carbon dust accretes below a certain threshold gas temperature, $T_{\text{gas}} = 1100$ K. For such a gas temperature the sublimation process of carbon grains is usually not at work. Iron dust does not react with H_2 molecules and only sublimation is included in the decomposition term for this dust species. For SiC chemisputtering is more efficient than pure sublimation and is included in the decomposition term.

We define the condensation radius of a certain dust species, i , $R_{c,i}$, as the distance at which $J_i^{\text{gr}} \geq J_i^{\text{dec}}$. In the case of carbon dust, the condensation radius is depending on the gas temperature profile that is also dependent on the amount of dust produced through equation (4).

(iii) Expansion velocity profile for a spherically symmetric, stationary outflow:

$$v \frac{dv}{dt} = -\frac{GM}{r^2} (1 - \Gamma), \quad (6)$$

where G is the gravitational constant and the quantity

$$\Gamma = \frac{L}{4\pi c GM} \kappa \quad (7)$$

is the ratio between the radiation pressure and the gravitational pull of the star. The constant c is the speed of light.

Equations 4, 5 (one equation for each dust species) and 6 provide the complete set of differential equations to integrate.

(iv) Gas profile, described by the mass conservation equation:

$$\rho = \frac{\dot{M}}{4\pi r^2 v}, \quad (8)$$

where the velocity, v , changes along the CSE according to equation (6).

(v) The dust-to-gas ratio, δ_i , for any of the dust species, i :

$$\delta_i = \frac{X_{k,i} f_i m_i}{m_{k,i} n_{k,i}}, \quad (9)$$

where $X_{k,i}$ is the mass fraction of the key element,¹ $m_{k,i}$ is its atomic mass, f_i is the number fraction of condensed key element particles over the total, $n_{k,i}$ is the number of atoms of the key element in one monomer of dust and m_i is the mass of the monomer. The quantity f_i for each dust species is computed following the grain growth in equation (5) and it changes along the CSEs.

(vi) Dust density profile, derived from equation (8):

$$\rho_{\text{dust}} = \rho \sum_i \delta_i. \quad (10)$$

(vii) Dust mass-loss rate, given by the contribution of all the dust species, i ,

$$\dot{M}_{\text{dust}} = \sum_i \dot{M}_i = \dot{M} \delta_i. \quad (11)$$

(viii) Total gas-to-dust ratio Ψ_{dust} , given by the ratio between the gas and dust mass-loss rates:

$$\Psi_{\text{dust}} = \frac{\dot{M}}{\dot{M}_{\text{dust}}}. \quad (12)$$

For the a posteriori radiative transfer calculation, the input quantities are the following.

(i) The optical depth at a given wavelength is computed as

$$\tau_\lambda = \frac{3\dot{M}}{4} \int_{R_c}^{\infty} \sum_i \frac{Q_{\text{ext},i}(\lambda, a_i) \delta_i(r)}{a_i \rho_i r^2 v(r)} dr, \quad (13)$$

where R_c is the condensation radius of the first dust species condensed, expressed in units of stellar radii R_* , and \dot{M} is assumed to be constant. The quantity Q_{ext} is the dust extinction coefficient, defined as

$$Q_{\text{ext}}(a_i, \lambda) = Q_{\text{abs},i}(a_i, \lambda) + Q_{\text{sca},i}(a_i, \lambda) - g Q_{\text{sca},i}(a_i, \lambda), \quad (14)$$

where g is defined as $g = \langle \cos \theta \rangle$ and θ is the scattering angle. The quantity $g Q_{\text{sca},i}(a_i, \lambda)$ provides the degree of forward scattering.

The quantities $Q_{\text{abs}}(a_{\text{amC}}, \lambda)$ and $Q_{\text{sca}}(a_{\text{amC}}, \lambda)$ are computed from the n , k optical constants under the assumption of spherical dust grains by means of the code `BHMIE` by Bohren, Huffman & Kam (1983), based on the Mie theory.

(ii) Dust temperature at the inner boundary of the shell, T_{inn} .

The code MoD can only deal with a single temperature for all the dust species formed. We take as representative temperature the carbon dust temperature at its condensation radius ($R_{c,\text{amC}}$) plus one stellar radius, as explained in Nanni et al. (2016). Carbon dust in

¹ The least abundant of the elements in the stellar atmosphere forming a given type of dust.

Table 2. Input stellar parameters and spacing for the dust formation calculations.

Parameter	Range/values	Spacing
$\log(L/L_{\odot})$	[3.2, 4]	0.1
	[4.0, 4.4]	0.05
$\log(\dot{M}/M_{\odot} \text{ yr}^{-1})$	[-7, -5]	0.1
	[-5.0, -4.4]	0.05
T_{eff}/K	[2500, 4000]	100
M/M_{\odot}	0.8, 1.5, 3	
C_{ex}	8.0, 8.2, 8.5	
C/O	1.65, 2, 3	
Z	0.004	

fact is usually the most abundant of the dust species formed in carbon-rich stars. The carbon dust temperature is computed from the balance between the absorbed and emitted radiation.

(iii) Optical quantities representative for the dust mixture:

$$\bar{Q}_{\text{ext}} = \frac{\sum_i \dot{M}_i Q_{\text{ext},i}(a_i, \lambda)}{\sum_i \dot{M}_i}, \quad (15)$$

where $Q_{\text{ext},i}(a_i, \lambda)$ is computed for the final grain size of each species, i , obtained by our dust formation model.

2.2 Grids of dusty models

We select the six combinations of optical data sets and grain sizes for amorphous carbon dust listed in Table 1 and discussed in Nanni et al. (2016). For SiC and metallic iron the optical data sets are fixed. Different assumptions of optical data sets and grain sizes yield different inner temperatures for the dust zone and different values of optical depth at $\lambda = 1 \mu\text{m}$, τ_1 , for the same input of the stellar quantities, because of different optical properties.

We then built six grids of models (one for each of the opacity set) by selecting a large range of stellar luminosity and mass-loss rates and some selected values of the actual stellar mass and carbon excess, $C_{\text{ex}} = \log(\epsilon_{\text{C}} - \epsilon_{\text{O}}) + 12$. The adopted metallicity is $Z = 0.004$ with scaled solar abundances for the elements in the atmosphere (excluding carbon).

The range and spacing of the stellar parameters are summarized in Table 2. They cover typical values for TP-AGB stars as predicted by stellar evolutionary models (Marigo et al. 2013, 2017). We compute the grids for all the effective temperatures available in the new grid of photospheric spectra presented in Aringer et al. (2016). The values of C/O have been interpolated in the grid of photospheric spectra for a metallicity value suitable for SMC stars. We limit our calculation to spectra for which the combination of the stellar parameters produces models with $10^{-3} \leq \tau_1 \leq 30$.

The grids of dusty spectra and dust properties are publicly available at <http://starkey.astro.unipd.it/web/guest/dustymodels>.

The data provided in the online grids of models consist on the input stellar quantities:

- mass-loss rate, \dot{M} , in $M_{\odot} \text{ yr}^{-1}$;
- current stellar mass, M , in M_{\odot} ;
- effective temperature, T_{eff} , in K;
- stellar luminosity, L , in L_{\odot} ;
- carbon excess, C_{ex} ;
- C/O ratio;
- metallicity, Z , in mass fraction.

The output quantities available for each combination of the input stellar parameters are:

- dust temperature at the inner boundary of the shell, T_{inn} in K;
- mass loss in dust for the different species, \dot{M}_{amC} , \dot{M}_{SiC} , \dot{M}_{iron} in $M_{\odot} \text{ yr}^{-1}$;
- outflow expansion velocity, v_{exp} , in km s^{-1} ;
- optical depth at different wavelengths, τ_{λ} ;
- spectrum reprocessed by dust, normalized for the total luminosity.

As an example, we show in Table 3 the first lines of the online tables. The format of the files containing the spectra is the default one provided by the code DUSTY (Ivezic & Elitzur 1997).

2.3 Comparison with previous approaches

Without a description for dust formation, the optical depth is estimated from equation (13) by assuming (a) constant outflow velocity, v_{exp} , (b) fixed dust chemical composition for evaluating $\bar{Q}_{\text{ext}}(\lambda, a)$ in equation (15), (c) same grain size (or grain size distribution) for all the dust species, (d) a certain dust density, $\bar{\rho}_{\text{d}}$, averaged for all the dust species using \dot{M}_i as weight. Under the above assumptions, equation (13) reads as

$$\tau_{\lambda}(\text{approx}) = \frac{3\dot{M}_{\text{dust}}\bar{Q}_{\text{ext}}(\lambda, a)}{4aR_{\text{c}}v_{\text{exp}}\bar{\rho}_{\text{d}}}. \quad (16)$$

The total DPR for each of the sources, \dot{M}_{dust} , is then evaluated inverting equation (16) once the value of τ_{λ} is found from the SED fitting procedure:

$$\dot{M}_{\text{dust}} = \frac{\tau_{\lambda}(\text{approx})4aR_{\text{c}}v_{\text{exp}}\bar{\rho}_{\text{d}}}{3\bar{Q}_{\text{ext}}(\lambda, a)}. \quad (17)$$

The condensation radius R_{c} is usually consistently computed by assuming a certain dust temperature at the boundary of the inner shell.

In the grid of models by Groenewegen et al. (2007) the value of T_{inn} is set to be 1000 K. In the Grid of RSG and AGB Models (GRAMS) by Srinivasan et al. (2011), the value of R_{c} is independent of T_{inn} and is derived from the fitting procedure. The grain size are assumed to be all of the same size $a \approx 0.1 \mu\text{m}$ by Groenewegen et al. (2007). On the other hand, Srinivasan et al. (2016) assumed the grain size distribution by Kim, Martin & Hendry (1994). The average size of the distribution by Srinivasan et al. (2016) is around $a \approx 0.1 \mu\text{m}$. The value of $\bar{Q}_{\text{ext}}(\lambda, a)$ is of course both dependent on the optical data set adopted and by the grain size.

Table 3. Example of input and output quantities contained in the publicly available online tables.

\dot{M}	M	T_{eff}	L	C_{ex}	C/O	Z	T_{inn}	\dot{M}_{C}	...	v_{exp}	τ_{V}	...	Spectrum
3.16×10^{-7}	0.8	2700	15 850	8.5	3.06	0.004	1209	2.22×10^{-11}	...	4.0	0.012	...	Name1
3.98×10^{-7}	0.8	2700	15 850	8.5	3.06	0.004	1211	5.30×10^{-11}	...	4.2	0.031	...	Name2
5.01×10^{-7}	0.8	2700	15 850	8.5	3.06	0.004	1212	1.02×10^{-10}	...	6.7	0.063	...	Name3
6.31×10^{-7}	0.8	2700	15 850	8.5	3.06	0.004	1212	1.67×10^{-10}	...	9.5	0.101	...	Name4
7.943×10^{-7}	0.8	2700	15 850	8.5	3.06	0.004	1212	2.53×10^{-10}	...	12.2	0.152	...	Name5

The value of v_{exp} is either assumed to be $v_{\text{exp}} = 10 \text{ km s}^{-1}$ as in Groenewegen et al. (2009) or scaled with the stellar luminosity and the gas-to-dust ratio, Ψ_{dust} :

$$v_{\text{exp}} \propto \left(\frac{L}{L_{\odot}}\right)^{\alpha} \left(\frac{\Psi_{\text{dust}}}{200}\right)^{-\beta}, \quad (18)$$

where the quantity Ψ_{dust} can be either set equal to 200 for C-rich stars in the SMC (Groenewegen 2006; Groenewegen et al. 2007, 2009; Boyer et al. 2012; Gullieuszik et al. 2012; Srinivasan et al. 2016) or is determined employing some scaling relations (Bressan, Granato & Silva 1998; Marigo et al. 2008). The power α and β can be theoretically derived (Habing, Tignon & Tielens 1994) or empirically determined (van Loon 2006; Goldman et al. 2017).

In the works by Boyer et al. (2012) and Srinivasan et al. (2016) the value of the expansion velocity is assumed to be $v_{\text{exp}} = 10 \text{ km s}^{-1}$ for a star with luminosity $L = 30\,000 L_{\odot}$ and $\Psi_{\text{dust}} = 200$. The final DPR for each star is scaled according to equation (18).

Once the quantity \dot{M}_{dust} is evaluated through equation (17) the mass-loss rate is estimated by assuming a certain value of the gas-to-dust ratio.

Our dust formation scheme allows us to avoid some assumptions adopted in the previous calculations of dusty spectra models and grids. The most important difference with respect to the previous approach, relies on the consistent evaluation of τ_{λ} , Ψ_{dust} , v_{exp} . In particular, the optical depth at a given wavelength, condensation radius, dust temperature at the boundary of the dust condensation zone, dust-to-gas ratios and dust density and velocity profiles are computed by our code.

2.4 Sample of C-rich stars

Unless specific filters are used to probe the presence of either O- or C-bearing molecules (e.g. Palmer & Wing 1982; Boyer et al. 2013), the identification of C-rich stars in photometric samples is not straightforward. Fortunately, in the case of the Magellanic Clouds most of the C-rich stars are known to stand out in a particular region of the K_s versus $J - K_s$ colour–magnitude diagram (CMD); they are simply indicated as ‘C-stars’ in Boyer et al. (2011). These stars are only mildly reddened by the dust present in their CSEs. Stars more dust enshrouded are instead selected based on their MIR colours and are classified as ‘extreme’ (X-) stars. For 81 stars the spectra from *Spitzer*’s Infrared Spectrograph (IRS) are available (Ruffle et al. 2015).

In addition, the catalogue by Boyer et al. (2011) contains a distinct class of objects, called ‘anomalous’ AGBs (aAGBs) classified based on their position in the [8] versus $J - [8]$ diagram. Optical medium-resolution spectra were obtained by Boyer et al. (2015) using the AAOmega/2dF multi-object spectrograph (Lewis et al. 2002; Saunders et al. 2004; Sharp et al. 2006) for 273 sources, which included 246 aAGBs. On the basis of the analysis performed on the spectra of aAGBs, Boyer et al. (2015) concluded that nearly half of the aAGB sample is expected to consist of C-rich stars. We exclude from the present analysis the sample of aAGBs classified as O-rich and S based on the spectral classification, we include instead those for which the classification is uncertain.

We exclude from the SED fitting five sources classified as C-rich based on the photometry but not based on their IRS or optical spectra. On the other hand, we include in our analysis five sources photometrically classified as O-rich but as C-rich based on their optical spectra plus one source for which the spectral classification is uncertain. The DPRs of these latter sources are included in the C-stars sample.

Table 4. Number of fitted AGB stars taken from the catalogue by Srinivasan et al. (2016), listed for the different classes of stars, photometrically classified by Boyer et al. (2011). A further selection of the sources is based on their IRS or optical spectra, when available (see text).

Photometric classification	Number
C-stars	1709
X-stars	339
O-stars (C-spectrum)	5
O-stars (unknown spectrum)	1
aAGB	1092
FIR	11

The catalogue by Boyer et al. (2011) includes 360 sources classified as far-infrared (FIR) sources. This list has been cleaned by Srinivasan et al. (2016) on the basis of the IRS classification when available and taking into account the identifications of such sources from other studies. The remaining 33 FIR sources have been divided into seven groups on the basis of their SED shape and the information on optical/IR variability (see section 2.4.1 in Srinivasan et al. 2016). The FIR sources considered as evolved star candidates and included in the dust budget by Srinivasan et al. (2016) belong to groups from 1 to 4 (17 sources). Here we exclude the six FIR sources spectroscopically classified as O-rich by Ruffle et al. (2015).

The number counts of C-rich sources included in our SED fitting are shown in Table 4 by colour class.

In the catalogue by Srinivasan et al. (2016) the 2MASS NIR photometry is available together with the MIR Infrared Array Camera (IRAC), Multiband Imaging Photometer for *Spitzer* (MIPS) 24 μm , *Akari* (S11 and L15 filters) survey of the SMC (Ita et al. 2010), the *Wide-field Infrared Survey Explore* (WISE; W3 filter) All-Sky Data Release, the Magellanic Clouds Photometric Survey (MCPS; Zaritsky et al. 2002) for the U and B bands and the Optical Gravitational Lensing Experiment (OGLE) survey for V and I bands, plus the variability information (OGLE-III; Udalski et al. 2008).

For the NIR bands, the 2MASS photometry of the SAGE-SMC list is matched to data from the Infrared Survey Facility (IRSF; Kato et al. 2007) when the photometry is available.

For the MIR bands (IRAC and MIPS 24 μm bands), the two epochs of SAGE-SMC have been matched with S³MC epoch for each source.

2.5 SED fitting procedure

From each of our six grids of spectra we select the best-fitting model of the sources in Table 4 by computing the reduced χ^2 between the modelled and observed photometry, similarly to Groenewegen et al. (2009), Gullieuszik et al. (2012), Riebel et al. (2012) and Srinivasan et al. (2016):

$$\chi^2 = \frac{1}{N_{\text{obs}}} \sum_i \frac{(F_{i,\text{obs}} - F_{i,\text{th}})^2}{e_{i,\text{obs}}^2}, \quad (19)$$

where $F_{i,\text{obs}}$ and $F_{i,\text{th}}$ are the observed and predicted fluxes for the i band, $e_{i,\text{obs}}$ is the error of the observed flux and N_{obs} is the number of observed photometric points. The distance of the SMC assumed to compute $F_{i,\text{th}}$ is $d_{\text{SMC}} \approx 60 \text{ kpc}$ (de Grijs & Bono 2015). The minimum value of χ^2 , corresponding to the best-fitting model, is indicated as χ_{best}^2 .

For a few sources it is necessary to exclude some of the observed photometric points from the SED fitting procedure. The criteria for the photometry selection are described in Appendix A.

To evaluate the uncertainties of the quantities derived from the SED fitting procedure, we need to estimate the possible variations of the modelled fluxes due to the photometric errors and to the intrinsic stellar variability. While the photometric errors can usually be described by Gaussian distributions, for large-amplitude variables, with observations spanning longer than a period, the distribution of photometric points will have peaks at the extremes of the measured distribution – just as those expected from sinusoidal-like variations. It is however impossible to identify the dominant factor in determining the error distribution, without performing a star-by-star analysis of the likely periods, amplitudes and the time span of the observations in each passband. Therefore, as a compromise between the expected Gaussian and/or sinusoidal distributions, we decide to simply adopt a flat distribution of errors, distributed over the magnitude interval of the observations. This conservative assumption probably provides an upper limit to the actual error distribution.

We therefore generate 100 sets of N_{ph} random numbers, r_i , where N_{ph} is the number of photometric bands, extracted from a uniform distribution of values between -1 and 1 . For each star, we only consider the valid photometric points, i , and we add to our best-fitting spectrum the quantity $r_i e_{i,\text{obs}}$:

$$F_{i,\text{th+err}} = F_{i,\text{th}} + r_i e_{i,\text{obs}}. \quad (20)$$

For all the 100 sets of random generated numbers we then recalculate the χ^2 of $F_{i,\text{th+err}}$ through equation (19). We finally extract the minimum and the 34th χ^2 values corresponding to 1σ variation, which provides an estimate of variation of the χ^2 within 1σ ($\Delta\chi^2$).

We compute the quantity $\chi_{\text{max}}^2 = \chi_{\text{best}}^2 + \Delta\chi^2$ and we extract, for each star, the models in the grid with $\chi^2 \leq \chi_{\text{max}}^2$. We then compute the average value of each of the quantities for the valid models, i.e. expansion velocity, gas-to-dust ratio, as well as the input stellar quantities, i.e. luminosity and effective temperature. For estimating the uncertainties over each of the quantities, we calculate the dispersion σ from the average value. If the number of models with $\chi^2 \leq \chi_{\text{max}}^2$ is ≤ 3 , we assume as average value the quantity corresponding to the χ_{best}^2 while we set the uncertainty equal to zero.

3 RESULTS

3.1 Trends in the grids of dusty models

We here discuss some trends between the optical depth at $\lambda = 1 \mu\text{m}$, τ_1 , where the spectra of TP-AGB stars peak, and the main stellar parameters such as L , carbon excess, M , T_{eff} and mass-loss rate. We opt to show τ_1 because, as discussed in other works (e.g. Bressan et al. 1998; Nanni et al. 2016), the SED of a dust-enshrouded star is mainly shaped by this quantity. From equations (13) and (16) we can see that τ_1 is dependent on several quantities, such as δ_i , R_c and v_{exp} which, in turn, are correlated with the stellar parameters.

In Fig. 1 we plot τ_1 against \dot{M} for different L computed for R12 optical data set. Thick black lines represent the trends derived from our models, whilst the thin red lines are the linear fits between τ_1 and \dot{M} . The mass loss has large impact on the final optical depth, as can be also seen from equations (13) and (16). However, the dependence of τ_1 on the mass-loss rate depends on the value of the luminosity, with a flatter trend for larger luminosity. Such a trend depends on the fact that the fraction of the condensed dust, which determines δ_i in equation (13), is not constant in our models but changes as a function of the input stellar parameters.

In Figs 2 and 3, τ_1 is shown as a function of the luminosity and carbon excess, respectively, for different choices of the mass-loss

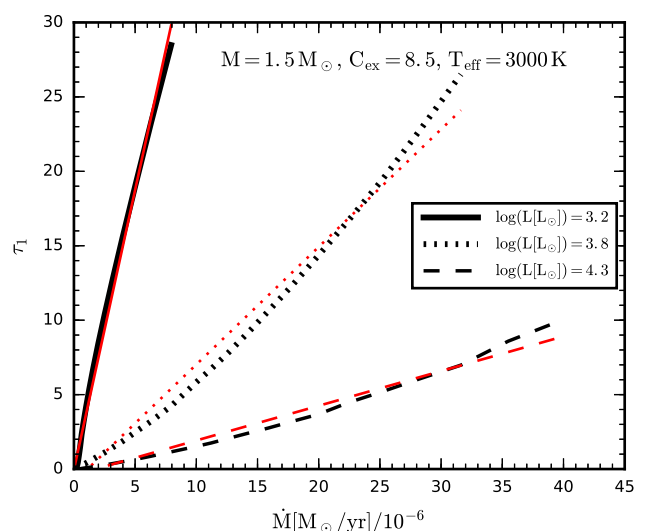


Figure 1. Optical depth at $1 \mu\text{m}$, τ_1 , as a function of mass-loss rate, for different choices of the luminosity, listed in the legend. Black thick lines are the trends derived from our models, whilst the corresponding red thin lines are the linear fit between τ_1 and \dot{M} . The models shown are computed with R12 optical data set for carbon dust. The other stellar parameters of the selected models are mentioned in the figure.

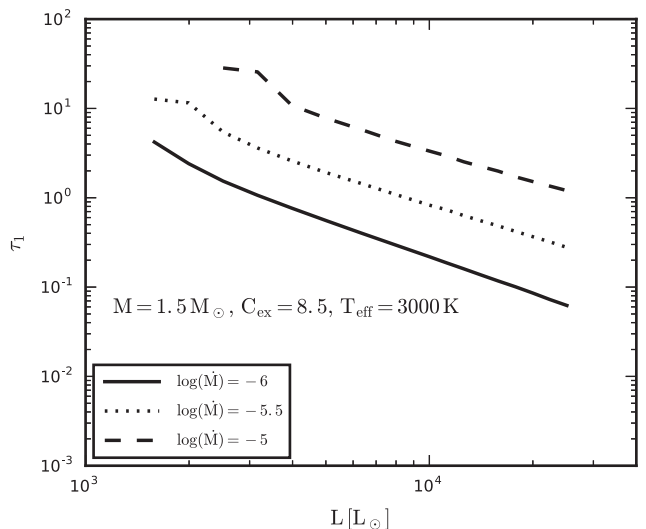


Figure 2. Optical depth at $1 \mu\text{m}$, τ_1 , as a function of luminosity, for different choices of the mass-loss rate, listed in the legend. The models shown are computed with R12 optical data set for carbon dust. The other stellar parameters of the selected models are mentioned in the figure.

rate. In these two figures, we show models computed for the R12 optical data set.

We can clearly see from Figs 2 and 3 that, for a given value of \dot{M} , the quantity τ_1 is mostly changed by the stellar luminosity, while the carbon excess usually produces only a secondary effect in the range of values considered, except for the smallest mass-loss rate. The strong dependence of τ_1 on the stellar luminosity is qualitatively in agreement with the scaling relations found by Bressan et al. (1998) and Ivezić & Elitzur (2010). We note, however, that the dependence of τ_1 on the quantity L is slightly stronger than the one predicted by Bressan et al. (1998) and Ivezić & Elitzur (2010). Assuming a dependence $\tau_1 \propto L^{-\alpha}$ we obtain $\alpha = -1.45, -1.22, -1.16$ for $\log \dot{M} = -6, -5.5, -5$, respectively, rather than $\alpha = -0.85$ of

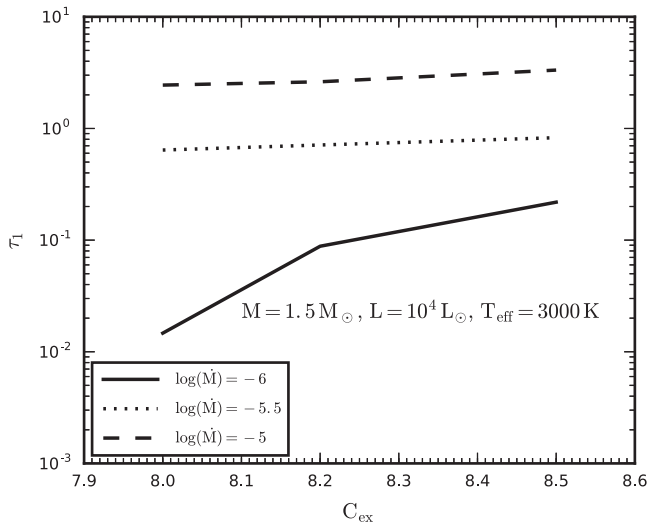


Figure 3. The same as Fig. 2, but with τ_1 as a function of carbon excess.

Bressan et al. (1998) or $\alpha = -1$ of Ivezić & Elitzur (2010). The dependence of τ_1 as a function of L is related to the behaviour of R_c , v_{exp} and δ_i as a function of L and for different mass-loss rates (equations 13 and 16). In particular, by inspecting the models shown in the figures, we find that R_c increases more steeply with L for the lowest mass-loss rate than for the larger ones, whilst the condensation fraction decreases more rapidly for the lowest mass-loss rate plotted. On the other hand, the outflow is not accelerated for $\log \dot{M} = -6$ so that the velocity does not depend on the luminosity for this specific case.

For the largest mass-loss rates considered, the velocity increases as a function of the luminosity and the condensation of dust is partially inhibited by the outflow acceleration, which dilutes the gas. However, the gas density is always large enough that the amount of dust condensed decreases less rapidly as a function of L than for the low mass-loss case. All these trends between the different stellar quantities and L explain the steeper dependence recovered between τ_1 and L for the lowest mass-loss rates with respect to the larger ones.

We always find a mild dependence of τ_1 on M , with τ_1 only slightly increasing as a function of the stellar mass. Finally, the effect of T_{eff} on τ_1 is also quite mild, even though for the largest mass-loss rates τ_1 tend to decrease for increasing T_{eff} .

3.2 Quality of the fit

The six grids of models produced are able to provide a good SED fit for most of the sources. In order to guarantee a good estimate of the total DPR, we analyse the χ^2_{best} of the most dust-producing stars among the C- and X-stars, yielding ≈ 80 per cent of the total DPR. The procedure is similar to the one applied by Srinivasan et al. (2016). The χ^2_{best} of these sources is $\lesssim 1$ for the ≈ 42 – 52 per cent of the sample considered and $\lesssim 10$ in the ≈ 94 – 98 per cent of the cases. Only one among the most dust-enshrouded stars (IRAS 00350–7436) is very poorly fitted by all the optical data sets of carbon dust ($\chi^2_{\text{best}} > 100$). This source has also been suggested to be a post-AGB star by Matsuura et al. (2005) and was discussed by Srinivasan et al. (2016), who also were not able to provide a good fit.

In Figs 4 and 5 we show two examples of well-fitted C-rich stars, with $\chi^2_{\text{best}} \approx 0.1$, and two examples of stars with a poor fit,

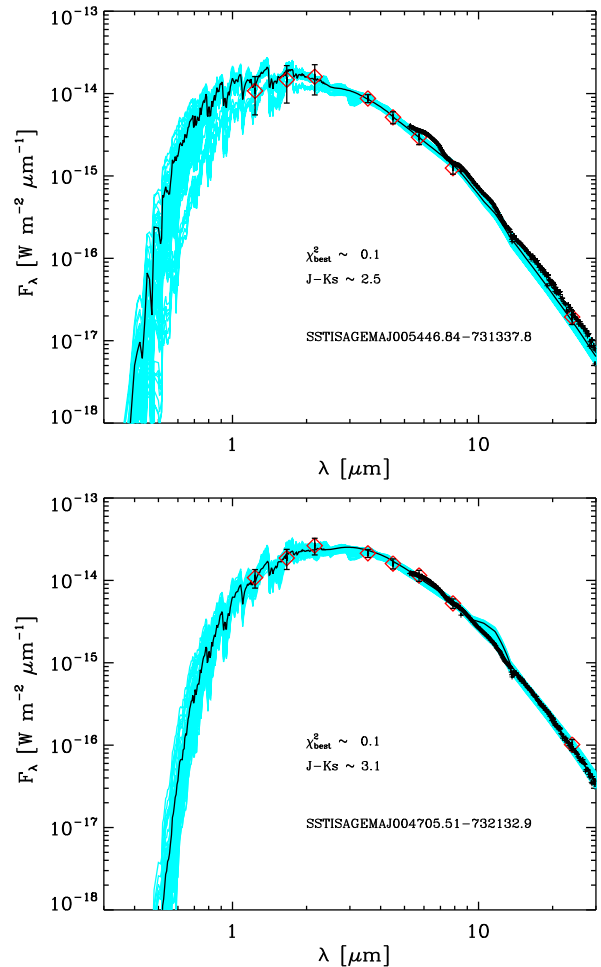


Figure 4. Two examples of carbon-rich stars well fitted with R12 data set for carbon dust. Red diamonds represent the valid observed photometric data points, overplotted with their uncertainties (error bars). The black solid lines represent the best-fitting spectra. The spectra overplotted in cyan correspond to models producing an acceptable χ^2 , as explained in the text. The values of $J - K_s$ and χ^2_{best} for each star are written in the figures. The IRS spectrum of each star is also overplotted with black crosses.

respectively. The valid observed photometric data points and uncertainties are plotted with red diamonds, whilst the photometric points, excluded with the criteria described in Appendix A, are plotted with green triangles. The IRS spectrum of each source has been overplotted when available (black crosses). The solid black line is the theoretical spectrum from our grid of models corresponding to the best fit. The cyan lines are the spectra of models producing a $\chi^2 \leq \chi^2_{\text{best}} + \Delta\chi^2$. In the upper panel of Fig. 5 the star previously discussed, IRAS 00350–7436, is shown.

For the aAGBs sample χ^2_{best} is $\lesssim 1$ and $\lesssim 10$ for about the ≈ 20 and ≈ 95 per cent of the cases, respectively. Even though Boyer et al. (2015) argued that half of these stars are possible oxygen-rich, we are able to provide an acceptable fit for all of them employing our carbon-rich models.

On the other hand, the fit is not always that satisfactory for the FIR, with $\chi^2_{\text{best}} \gtrsim 10$ for five sources.

3.3 Dust properties and stellar quantities

From the SED fitting procedure we can derive some important stellar quantities and dust properties.

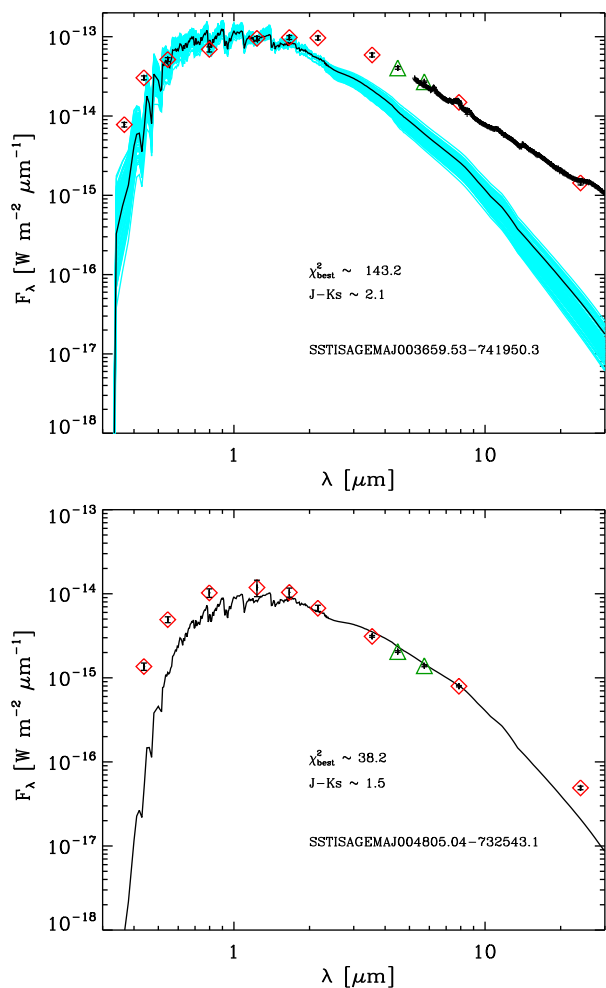


Figure 5. The same as Fig. 4, but for two carbon-rich stars not well fitted by the theoretical spectra. Red diamonds represent the valid observed photometric data points overplotted with their uncertainties, whilst the two green triangles are the photometric points excluded from the fit based on the criteria discussed in Appendix A. The source in the upper panel is IRAS 0035–7436, discussed in the text. No IRS spectrum is available for the source in the lower panel. Only one valid theoretical spectrum is derived from the analysis, drawn in solid black.

3.3.1 Luminosity function

In Fig. 6 the luminosity function of the C- and X-stars is shown. The optical data set selected is R12, but the result does not change significantly with a different data set. The absolute bolometric magnitude ranges between $M_{\text{bol}} \approx -3.2$ and ≈ -6.2 , while the peak of the distribution is around $M_{\text{bol}} \approx -4.5$. Our distribution is in excellent agreement with the one obtained by Srinivasan et al. (2016) through SED fitting applied to same sample of stars. For comparison we also show the luminosity function of C-stars in the SMC obtained from the catalogue of Rebeiro, Azzopardi & Westerland (1993), which includes 1707 C-stars identified on GRISM plates. We obtain the bolometric magnitudes from the visual magnitudes at 5220 Å using the corrections by Westerland, Azzopardi & Breyssacher (1986) and assuming a true distance modulus for the SMC $\mu_0 = 18.9$ mag. For consistency of comparison we exclude the faintest ($M_{\text{bol}} > -3.2$) C-stars from the Rebeiro et al. (1993) catalogue since our sample includes C-star brighter than the RGB tip. We note that the peak location of the luminosity function of Re-

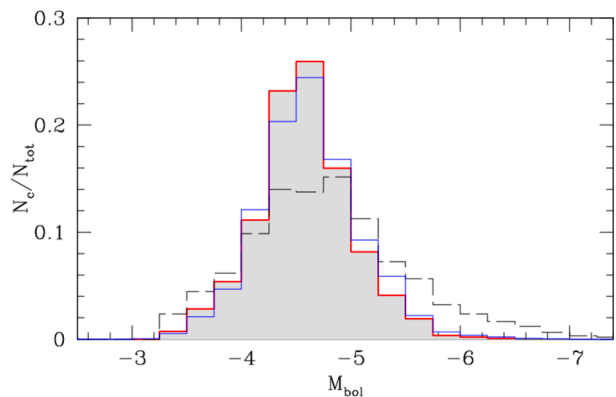


Figure 6. Luminosity function of C- and X-stars derived from the SED fitting procedure (red histogram shaded in grey). For comparison we plot the normalized distributions of C-stars obtained from the catalogue of Rebeiro et al. (1993) (dashed histogram), and that derived by Srinivasan et al. (2016) using their best-fitting luminosity estimates (blue histogram).

beiro et al. (1993) agrees with ours and with Srinivasan et al. (2016) at $M_{\text{bol}} \approx -4.5$, but the distribution is broader, extending towards fainter and brighter magnitudes. The reason for this difference is not clear, likely related to the different methods.

3.3.2 Mass-loss rates

In the six panels of Fig. 7 the linear, normalized density maps of all the sources are plotted against the $J - K_s$ colour. The different classes of stars are contour lined with different styles.

The mass-loss rates derived for aAGBs are typically lower than the ones of C-stars. The FIR sources are not located in a specific place in the diagram and their position depends on $J - K_s$. The separation between C- and X-stars occurs around $\log \dot{M} \approx -6$ at $J - K_s \approx 2$. Stars with $J - K_s \gtrsim 3$ reach the largest mass-loss rates of $-4.6 \lesssim \log \dot{M} \lesssim -4.4$, where the exact values depend on the optical data set considered.

The mass-loss rates for the different classes of stars with R13 and H11 are, respectively, the largest and the lowest derived by our analysis. With R13 we obtain $\log \dot{M} \approx -6.3$ for aAGBs, $-6.2 \lesssim \log \dot{M} \lesssim -5.8$ for C-stars and $-5.6 \lesssim \log \dot{M} \lesssim -4.8$ for X-stars. For H11, aAGBs are located around $\log \dot{M} \approx -6.8$, C-stars in the range $-6.8 \lesssim \log \dot{M} \lesssim -6.3$ and X-stars in the range $-5.9 \lesssim \log \dot{M} \lesssim -5.2$. For R12, J1000, Z12 and J400 each class of stars occupies approximately the same region in the plot. For these data sets, aAGBs are concentrated around $\log \dot{M} \lesssim -6.4$, whilst most of the C- and X-stars are located in the range $-6.5 \lesssim \log \dot{M} \lesssim -6$ and $-5.8 \lesssim \log \dot{M} \lesssim -5$, respectively.

The uncertainty affecting the mass-loss estimate is between ≈ 10 and ≈ 60 per cent for the least dust-rich stars and between ≈ 20 and ≈ 40 per cent for dust-enshrouded stars.

In Fig. 8 we plot the ratio of the mass-loss rates derived for R13 and H11, as a function of the $J - K_s$. As discussed before, these two data sets yield the maximum and minimum typical values of the mass-loss rates. The figure points out that the mass-loss rates of the least dusty stars are typically between ≈ 1.5 and 5 times larger for R13, whilst, for the dustiest stars, the mass-loss rate is typically a factor of ≈ 2 larger for R13. For few C-stars, not visible in the density plot, the mass-loss rates derived with R13 can be up to ≈ 7 – 8 times larger than the ones obtained with H11. Larger mass losses for the R13 data set imply that a higher density than for H11 is needed to produce approximately the same dust extinction.

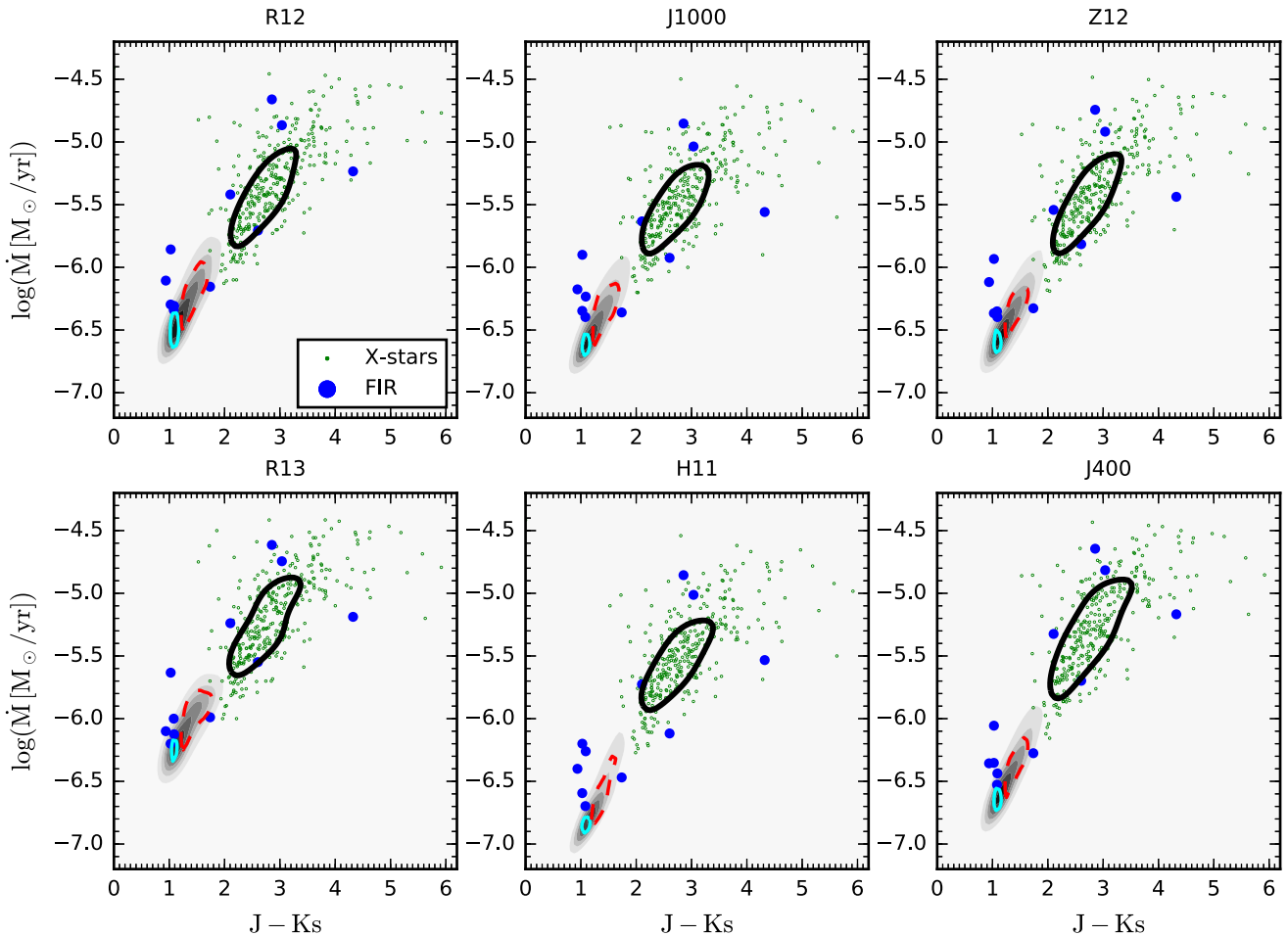


Figure 7. Mass-loss rate as a function of the $J - K_s$ colour derived from the SED fitting procedure for the different optical data sets. The linear normalized density map from 0, light grey, to 1, black, includes all classes of stars. X- and FIR stars are overplotted with different colours and symbols listed in the legend. C-, X- and aAGB stars are also contour plotted with different colours and line styles: dashed red for C-stars, solid black thick for X-stars and solid cyan thin for aAGBs.

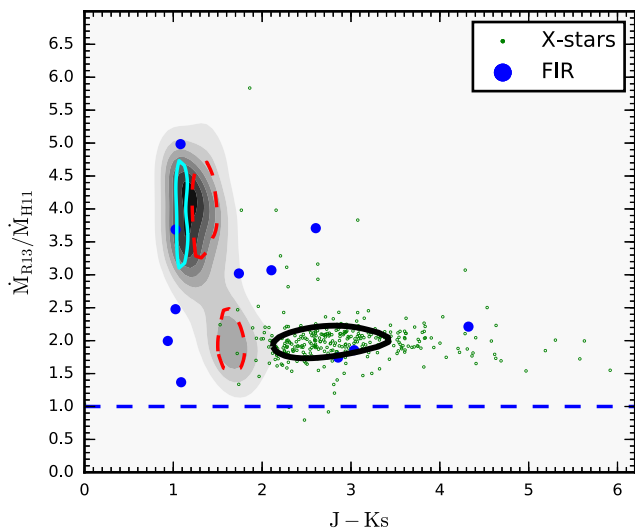


Figure 8. Ratios between the mass-loss rates derived for R13 and H11 data sets as a function of $J - K_s$ colour. The colour code for the different classes of stars is the same as in Fig. 7. The blue dashed line indicates a constant ratio, =1, corresponding to the same mass-loss rate for the two data sets.

In Fig. 9 the normalized distributions of mass-loss rates derived for all the optical data sets are shown for both groups of C- and X-stars. These two classes of stars are compared to those of a Galactic samples taken from the literature. Dust-enshrouded stars are taken from Groenewegen et al. (2002), while optically bright C-stars are from Schöier & Olofsson (2001). The most dusty stars in our Galaxy share comparable distributions with X-stars in the SMC, especially for R13 and J400 data sets, even though the peak of the SMC distribution is shifted to lower values of the mass-loss rates. Optically bright C-stars in the SMC are characterized by somewhat larger mass-loss rates compared to the Galactic ones, whose distribution is broader and extends down to lower values. The only exception is represented by H11, for which the mass-loss distribution of C-stars in the SMC is similar to the one of optically bright Galactic sources.

3.3.3 Gas-to-dust ratios

We consistently derived the values of the gas-to-dust ratio (equations 9, 11 and 12) and the associated uncertainties for the fitted stars.

In Fig. 10 we show the gas-to-dust ratios as a function of the mass-loss rate for all the optical data sets. The value of Ψ_{dust} can differ considerably from the constant value of 200 usually adopted

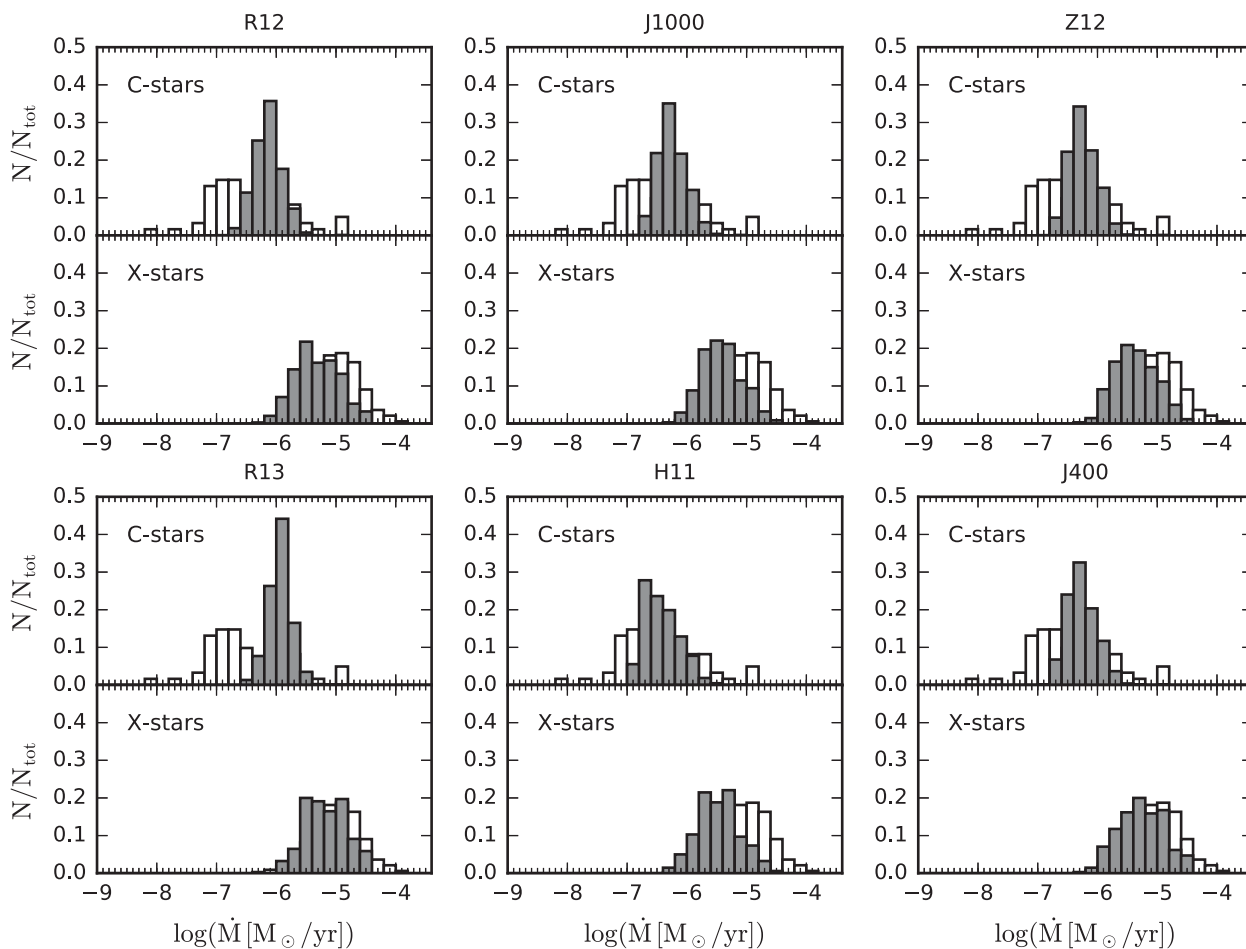


Figure 9. For each chart, upper panel, the normalized distribution of mass-loss rates for the stars in the SMC (shaded histogram) is compared to that of a volume-limited sample of Galactic optically bright C-stars from Schöier & Olofsson (2001) (white histogram). In the lower panel of each chart, X-stars in the SMC are compared to a sample of Galactic highly obscured C-stars (Groenewegen et al. 2002).

(Groenewegen 2006; Groenewegen et al. 2007, 2009; Boyer et al. 2012; Gullieuszik et al. 2012; Srinivasan et al. 2016). In fact, Ψ_{dust} spans a large range of values, especially for the sources with $\log \dot{M} \lesssim -6$. The value of the mass-loss rate $\log(\dot{M}) \approx -6$ ($J - K_s \approx 2$) roughly corresponds to the separation between C- and X-stars, appearing around $\Psi_{\text{dust}} \approx 800\text{--}2000$, depending on the optical data set. For $\log \dot{M} \lesssim -6$, Ψ_{dust} increases steeply as a function of the mass-loss rate with progressively less dust in CSEs. Stars with $\log \dot{M} \gtrsim -6$ form dust more efficiently in their CSEs. This result indicates that dust condensation is more efficient in denser environments, which correspond to larger values of the mass-loss rate. Furthermore, the dependence between Ψ_{dust} and the mass-loss rate is much milder than for $\log \dot{M} \gtrsim -6$ and Ψ_{dust} tends to saturate. Most of X-stars have gas-to-dust ratios of $800 \lesssim \Psi_{\text{dust}} \lesssim 2000$, depending on the selected opacity. The quantity Ψ_{dust} for X-stars derived with R12 and J400 is less scattered than the other data sets. The lowest value of Ψ_{dust} also depends on the opacity adopted, but it is usually no lower than ≈ 500 , with only few exceptional stars. In any case, Ψ_{dust} is never as low as the value of 200, usually assumed in the literature.

The predicted values of Ψ_{dust} of aAGBs are much larger than the ones of C- and X-stars, as also expected from the analysis performed by Boyer et al. (2011). Anomalous AGBs are in fact expected to be very inefficient dust producers. On the other hand, FIR sources are not placed in specific regions of the plots.

The uncertainty associated with the gas-to-dust ratio is larger for the least dusty stars, usually between ≈ 20 and ≈ 80 per cent, whilst it is between ≈ 30 and ≈ 40 per cent for the dustiest sources. The largest uncertainty in the gas-to-dust ratio for the least dust-enshrouded stars is not surprising, since large values of the gas-to-dust ratio are always expected to correspond to almost dust-free spectra, which yield equally good fits for almost dust-free stars.

In Fig. 11 we show the ratio between Ψ_{dust} obtained with R13 and R12. These data sets yield among the most different values of Ψ_{dust} , especially for the dustiest stars. For the least dusty stars, the gas-to-dust ratio for R13 is between ≈ 1.2 and ≈ 2.8 times larger than the one obtained with R12. For some sources, not visible in the density plot, Ψ_{dust} is up to ≈ 7 times larger for R13. For X-stars, the Ψ_{dust} of R13 is usually between ≈ 40 and ≈ 90 per cent larger than the one of R12. This result implies that dust condensation is expected to be more efficient if the type of dust formed has optical constant similar to R12 rather than R13.

The spread in the values of Ψ_{dust} predicted by our analysis is also found in the most updated grid of dynamical models by Eriksson et al. (2014), in which the value of Ψ_{dust} can vary by a factor of 30, with $330 \lesssim \Psi_{\text{dust}} \lesssim 10000$. The value of Ψ_{dust} is expected to be related to the carbon excess, with lower Ψ_{dust} for larger values of the carbon excess (Mattsson, Wahlin & Höfner 2010; Nanni et al. 2013; Eriksson et al. 2014). This result again shows that a unique value

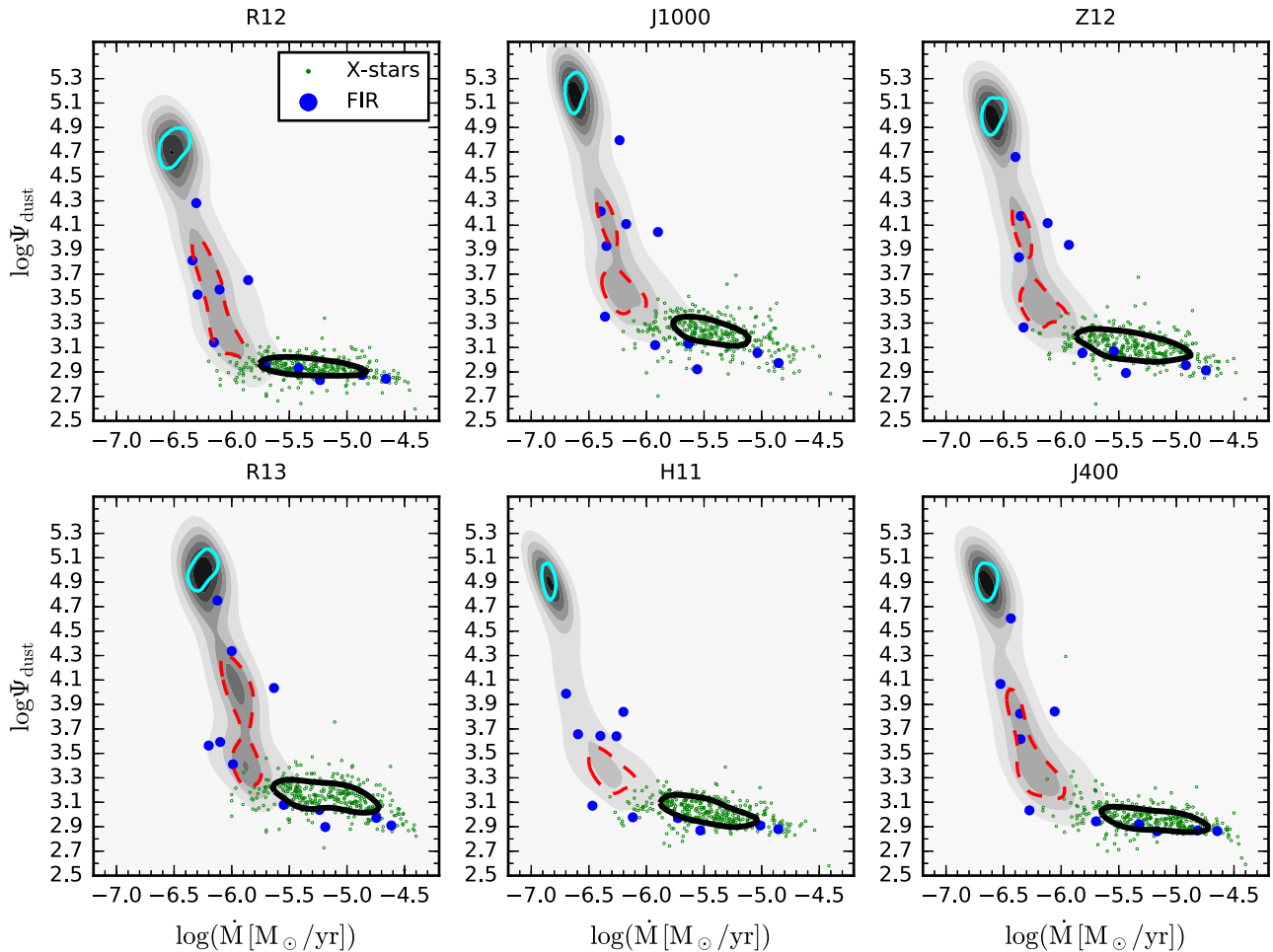


Figure 10. Gas-to-dust ratio as a function of the mass-loss rate for all the optical data sets of carbon dust. The colour code for the different classes of stars is the same as in Fig. 7.

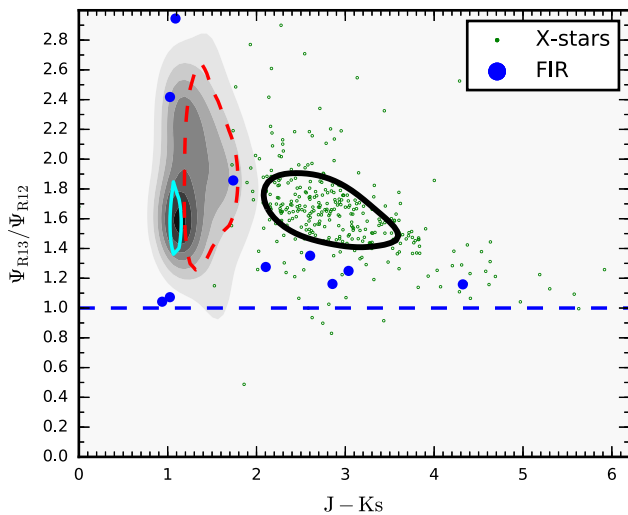


Figure 11. Ratios between the values of Ψ_{dust} derived for R13 and R12 data sets as a function of $J - K_s$ colour. The colour code for the different classes of stars is the same as in Fig. 7. The blue dashed line indicates a constant ratio, =1, corresponding to the same value of Ψ_{dust} rate for the two data sets.

of Ψ_{dust} for all the C-rich sources might not be a realistic choice, as also noticed by Eriksson et al. (2014).

3.3.4 Dust chemistry

The growth of all the dust species included in our model (amorphous carbon, SiC and metallic iron) is followed with equation (5). Since the growth rate of a certain dust species is proportional to the number density of the dust-forming molecules in the CSEs, we expect the mass fraction of SiC and iron to be dependent on the starting abundance of Si and Fe atoms, respectively, on the density of the outflow, determined through the mass-loss rate and the velocity (equation 8), and on formation sequence of the dust species. The abundances of Si and Fe depend on the metallicity of the SMC. On the other hand, the formation of carbon dust is, in many cases, able to accelerate the outflow and to reduce the density. The condensation sequence of dust in our model, usually predicts SiC to form first, before that the outflow acceleration, followed by amorphous carbon and iron. This latter dust species is formed after that the outflow is accelerated, when this process occurs. Similarly to the amorphous carbon dust, the final grain sizes of SiC and iron are also dependent on the seed particle abundance.

In Fig. 12 the mass fractions of SiC over the total dust produced are plotted against $J - K_s$ for R12 data set. The trend found is not much dependent on the adopted set of optical constants. This figure

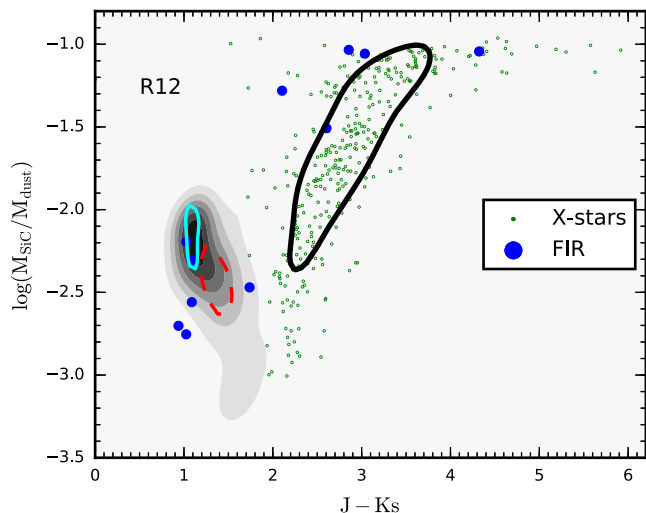


Figure 12. SiC mass fraction as a function of $J - K_s$ derived with R12 optical data set. The colour code for the different classes of stars is the same as in Fig. 7.

highlights a trend between the SiC mass fraction and $J - K_s$ for X-stars, which saturates around $J - K_s \approx 3$ and never becomes larger than ≈ 10 per cent. This trend suggests that more SiC is formed in denser environments, since larger values of $J - K_s$ correspond to larger mass-loss rates. In fact, since SiC forms before carbon dust, this dust component forms before the onset of the dust-driven wind and more condensation is expected for larger densities. On the other hand, the mass fraction of SiC is limited by the initial abundance of Si, dependent on the metallicity. As a consequence, an upper value of the SiC mass fraction is attained around $J - K_s \approx 3$. For less dust-rich stars, a reversed trend between the SiC mass fraction and $J - K_s$ is visible. However, since the values are always below ≈ 1 per cent the trend is not well defined. The uncertainty associated with the SiC mass fraction can be large even for dust-enshrouded stars. For $J - K_s \approx 3$ the uncertainty is between ≈ 20 and ≈ 100 per cent and it decreases with $J - K_s$, down to ≈ 30 per cent.

We do not find a clear trend between the iron dust mass fraction with the $J - K_s$ colour, and its fraction is always below 1 per cent for all the classes of stars. The low amount of iron dust is an expected result, since this dust species is formed later than amorphous carbon when to the outflow density decreases following the accelerated expansion.

3.3.5 Grain sizes

In Fig. 13 we plot the size of carbon grains obtained for the sources fitted with R13 against $J - K_s$ for the different classes of stars. Stars with increasing dust content attain larger grain sizes. For R13 data set, amC dust grains in CSEs of aAGBs are usually around $0.03 \lesssim a_{\text{amC}} \lesssim 0.04 \mu\text{m}$. On the other hand, the bulk of C- and X-stars are fitted with models with final grain sizes in the range $0.06 \lesssim a_{\text{amC}} \lesssim 0.1$ and $0.11 \lesssim a_{\text{amC}} \lesssim 0.14 \mu\text{m}$, respectively. The maximum grain size is attained for the reddest X-stars and is around $\approx 0.16 \mu\text{m}$.

As discussed in Nanni et al. (2016), the final grain size is mostly dependent on the choice of the seed particle abundance and is expected to roughly follow the relation

$$a_i \propto (\epsilon_s)^{-1/3}, \quad (21)$$

where ϵ_s is the adjustable parameter of equation (1). The grain sizes are therefore expected to be a factor of ≈ 2 smaller than the ones of

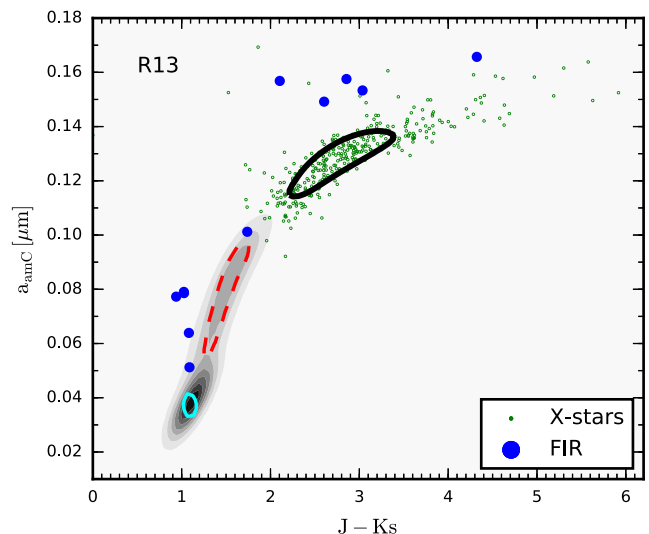


Figure 13. Size of carbon grains as a function of the $J - K_s$ colour derived for R13 optical data set. The colour code for the different classes of stars is the same as in Fig. 7.

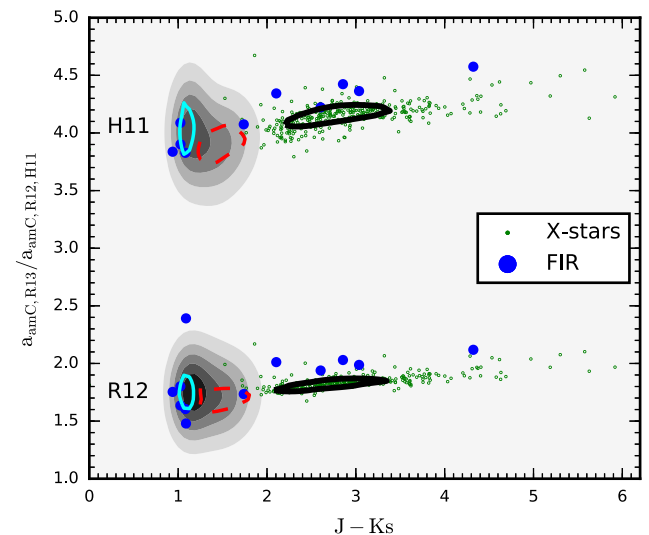


Figure 14. Ratios between the grain sizes obtained with R13 and the ones derived from H11 and R12 as a function of the $J - K_s$ colour. The colour code for the different classes of stars is the same as in Fig. 7.

R13, if $\log(\epsilon_s) = -12$ (R12, Z12, J400, J1000), and ≈ 4.6 smaller, if $\log(\epsilon_s) = -11$ (H11). In Fig. 14 we show the ratios between the grain sizes obtained with R13 and the ones derived from H11 and R12, as a function of $J - K_s$. From the figure we conclude that the expected scaling factors between the grain sizes are roughly recovered.

The final grain sizes obtained from our models are clearly different between the various classes of stars and can be also very different from the value of $a_{\text{amC}} \approx 0.1 \mu\text{m}$ usually adopted in the literature.

For all the optical data sets considered, the uncertainty associated with the size of carbon grains is usually below few per cents and anyway within ≈ 30 per cent, for the least dust-enshrouded stars, while is always around 3–4 per cent for the reddest stars.

The trend of SiC grain size as a function of $J - K_s$ is qualitatively similar to the one recovered for carbon dust, but the final size of

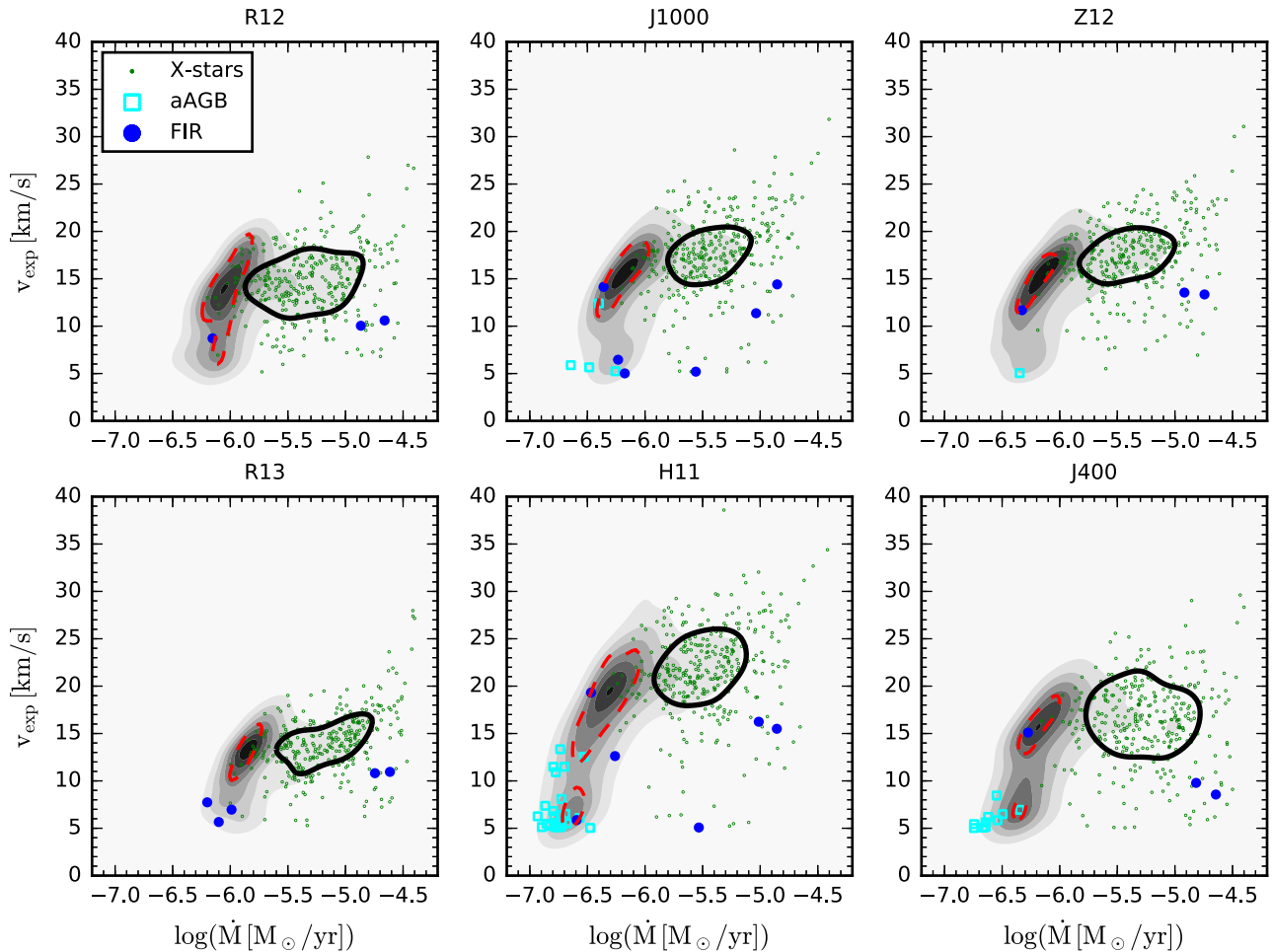


Figure 15. Expansion velocity as a function of the mass-loss rate for all the optical data sets of carbon dust. The colour code for the different classes of stars is the same as in Fig. 7.

SiC grains is always $\lesssim 0.04 \mu\text{m}$. The reason for this low value of the grain size is that SiC is limited by the silicon abundance. The uncertainty associated with the SiC grain size is typically between ≈ 10 and ≈ 40 per cent for the least dust-enshrouded stars and it decreases for the dustiest stars, down to ≈ 15 per cent.

3.3.6 Expansion velocities

In this section we discuss the expansion velocities obtained by our SED fitting procedure.

In Fig. 15 the expansion velocities against the mass-loss rates are plotted for all the optical data sets. Only the stars for which the outflow is accelerated ($v_{\text{exp}} \geq 5 \text{ km s}^{-1}$) are shown.

For all the data sets, the expansion velocity increases with the mass-loss rate for C-stars and it flattens for X-stars attaining a maximum value around $-5.7 \lesssim \log(\dot{M}) \lesssim -5.6$. The scatter of the velocities of X-stars is always large. Because of the low amount of dust produced in their CSEs, few aAGBs are accelerated through dust-driven wind, but only for H11, J1000 and J400. FIR sources show different velocities that are related to the dust content in their CSEs. The dust-driven wind is sustained for different minimum values of the mass-loss rate for the different optical data sets.

The trends of the expansion velocity and the density distributions of the stars are similar for J1000, Z12 and J400. Among these data sets, the scatter of the velocities of X-stars obtained with J400

is the largest. The bulk of C-stars shows velocities of $11 \lesssim v_{\text{exp}} \lesssim 19 \text{ km s}^{-1}$ and mass-loss rates $-6.5 \lesssim \log(\dot{M}) \lesssim -6$. For mass-loss rates lower than $\log(\dot{M}) \lesssim -6.5$ ($\lesssim -6.7$ for J400) the outflow is not efficiently accelerated. Most of X-stars show velocities in the range $15 \lesssim v_{\text{exp}} \lesssim 21 \text{ km s}^{-1}$ for J1000 and Z12 and $13 \lesssim v_{\text{exp}} \lesssim 21 \text{ km s}^{-1}$ for J400 with $-6 \lesssim \log(\dot{M}) \lesssim -5$. Only few, heavily mass-losing stars, exhibit velocities up to $v_{\text{exp}} \approx 30 \text{ km s}^{-1}$.

For R12 data set, the velocities of C-stars are similar to J1000, Z12 and J400, but the bulk of these stars shows larger mass-loss rates $-6.2 \lesssim \log(\dot{M}) \lesssim -5.8$. The mass-loss required for accelerating the outflow is also slightly larger with respect to the ones previously discussed. On the other hand, X-stars reach slightly lower expansion velocities, usually below $\approx 20 \text{ km s}^{-1}$ for $-6 \lesssim \log(\dot{M}) \lesssim -5$. Only few sources reach larger velocities, $v_{\text{exp}} \approx 27 \text{ km s}^{-1}$.

The velocities obtained with R13 are the lowest. For this data sets, the velocities of most of the C-stars are in the range $10 \lesssim v_{\text{exp}} \lesssim 16 \text{ km s}^{-1}$ with $-6 \lesssim \log(\dot{M}) \lesssim -5.8$. The minimum mass-loss rate for the wind acceleration is $\log(\dot{M}) \approx -6.2$. The majority of X-stars show velocities in the range $11 \lesssim v_{\text{exp}} \lesssim 17 \text{ km s}^{-1}$. Only few X-stars, with the largest mass-loss rates, attain velocities up to $25 \lesssim v_{\text{exp}} \lesssim 27 \text{ km s}^{-1}$.

The velocities derived with H11 are $12 \lesssim v_{\text{exp}} \lesssim 24 \text{ km s}^{-1}$ for most of the C-stars and are concentrated in a range of mass-loss rates broader than the ones of the other data sets, $-6.7 \lesssim \log(\dot{M}) \lesssim -6$. The outflow acceleration starts to be efficient at $\log(\dot{M}) \lesssim -6.9$.

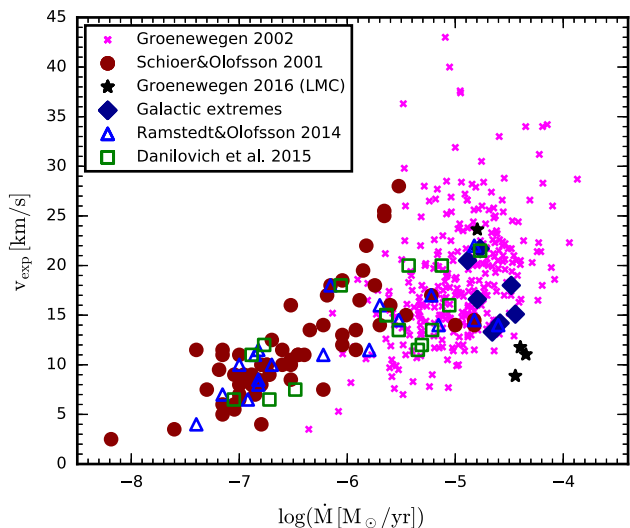


Figure 16. Expansion velocity as a function of the mass-loss rate of carbon stars in our Galaxy derived by different authors (Schöier & Olofsson 2001; Groenewegen et al. 2002; Ramstedt & Olofsson 2014; Danilovich et al. 2015; Groenewegen et al. 2016, table 4), and in the LMC (Groenewegen et al. 2016), represented with different colours and symbols listed in the legend. Stars named as ‘Galactic extreme’ are taken from table 4 of Groenewegen et al. (2016).

The velocities of X-stars are the largest obtained and are concentrated around $19 \lesssim v_{\text{exp}} \lesssim 26 \text{ km s}^{-1}$. The maximum expansion velocity attained (for few sources) is up to $\approx 30\text{--}35 \text{ km s}^{-1}$.

The uncertainty associated with the expansion velocity is usually between ≈ 10 and ≈ 70 per cent for the least dusty stars, and between ≈ 30 and ≈ 40 per cent for most of the dustiest sources.

The panels of Fig. 15 are compared with observations, shown in Fig. 16. In this figure, the expansion velocities are plotted against the mass-loss rate derived from observations in our Galaxy (Schöier & Olofsson 2001; Groenewegen et al. 2002; Ramstedt & Olofsson 2014; Danilovich et al. 2015; Groenewegen et al. 2016, table 4, and references therein), and in the Large Magellanic Cloud (LMC; Groenewegen et al. 2016). The two samples in Groenewegen et al. (2002) and Groenewegen et al. (2016, table 4) are IR luminous, dust-rich sources. In particular, the stars in the sample in Groenewegen et al. (2016, table 4) have been named as ‘Galactic extreme’, as also reported in the figure. By comparing Figs 15 and 16, we can see that the trend between v_{exp} and \dot{M} derived for carbon stars in the SMC is quite similar to the one observed for Galactic sources.

The observed velocities of Galactic stars exhibit quite a large scatter, especially at the largest mass-loss rates. This effect is also predicted by our analysis for the SMC carbon stars. In the range of mass-loss rates $-7 \gtrsim \log \dot{M} \gtrsim -6.5$ the stars observed in our Galaxy already show expansion velocities of $6 \lesssim v_{\text{exp}} \lesssim 10 \text{ km s}^{-1}$. Similar velocities in the same range of mass-loss rates are only obtained for H11 in the SMC. Most of the Galactic stars exhibit velocities around $10 \lesssim v_{\text{exp}} \lesssim 20 \text{ km s}^{-1}$ for mass-loss rates of $-5.5 \gtrsim \log \dot{M} \gtrsim -4.5$. These values are also attained by SMC stars in a similar range of mass loss, with the exclusion of R13 data set, for which lower velocities are predicted. In the same range of mass-loss rates, some Galactic stars reach velocities in the range $20 \lesssim v_{\text{exp}} \lesssim 25 \text{ km s}^{-1}$, which are only achieved by SMC sources fitted with H11. The largest velocities observed for Galactic stars, $v_{\text{exp}} \approx 40\text{--}45 \text{ km s}^{-1}$, are never attained for the SMC stars.

Excluding the Galactic stars with $v_{\text{exp}} \gtrsim 25 \text{ km s}^{-1}$ and the ones with $-7 \gtrsim \log \dot{M} \gtrsim -6.5$, the observed velocities of C-rich stars

in our Galaxy are in general comparable to the ones derived for the SMC. This finding indicates that there is not a large difference in the predicted velocities of carbon stars for different metallicity. Our result is in line with the analysis performed by means of hydrodynamical simulations by Mattsson et al. (2010) and Eriksson et al. (2014). These authors concluded that the carbon excess, rather than metallicity, is one of the key parameters that determines the properties of the dust-driven wind of carbon stars. In particular, the expansion velocities predicted by theoretical models is expected to be dependent on the choice of the carbon excess, with larger expansion velocities for larger values of carbon excess.

In Fig. 17 we plot the expansion velocities ($v_{\text{exp}} \geq 5 \text{ km s}^{-1}$) as a function of the luminosity. For comparison, we show the expansion velocities obtained from the scaling relation in equation (18) (black squares), adopted in Boyer et al. (2012) and by Srinivasan et al. (2016) with the assumption $v_{\text{exp}} = 10 \text{ km s}^{-1}$ for $L = 30\,000 L_{\odot}$ and $\Psi_{\text{dust}} = 200$. The expansion velocity correlates with the luminosity, as predicted by the theory of dust-driven wind (Elitzur & Ivezić 2001; Ivezić & Elitzur 2010). For all the data sets, the outflow acceleration occurs at about the same value of the luminosity, $L \approx 2000 L_{\odot}$. The linear trend between the velocity and luminosity is particularly evident for the dustiest stars, which reach their maximum expansion velocity for the largest luminosity, $L \approx 25\,000 L_{\odot}$.

In Fig. 18 we plot the observed velocities as a function of the luminosity for the same Galactic and LMC samples of Fig. 16. By comparing Figs 17 and 18 we can immediately see that the trend between the velocity and luminosity for the SMC stars is similar to the one observed for Galactic stars. Some of the observed Galactic sources have $2 \lesssim v_{\text{exp}} \lesssim 10 \text{ km s}^{-1}$ just above $2000 L_{\odot}$ (Schöier & Olofsson 2001). This result is usually in line with the one obtained for SMC stars. Around $L = 6000 L_{\odot}$, the observed velocities of Galactic stars are $6 \lesssim v_{\text{exp}} \lesssim 18 \text{ km s}^{-1}$. These values are similar to the ones of SMC stars for all the data sets. The bulk of the Galactic stars with the largest velocities is around $8000 \lesssim L \lesssim 9000 L_{\odot}$. At these luminosities the velocities attained by SMC stars are in the range $20 \lesssim v_{\text{exp}} \lesssim 25 \text{ km s}^{-1}$, similarly to most of the Galactic stars. Lower velocities are expected by adopting R13, whilst by employing H11 the velocities are up to $v_{\text{exp}} \approx 28 \text{ km s}^{-1}$. Velocities up to $v_{\text{exp}} \approx 40\text{--}45 \text{ km s}^{-1}$ are reached for some of the Galactic stars at $8000 \lesssim L \lesssim 10\,000 L_{\odot}$, whereas the maximum value reached by our models is $v_{\text{exp}} \approx 39 \text{ km s}^{-1}$ for higher luminosities $L \approx 25\,000 L_{\odot}$ and only with H11.

We again find that the dynamical properties of SMC carbon stars are in general comparable to the ones of Galactic sources and they are not significantly related to the initial metallicity.

In Fig. 19 we plot the average velocities of the stars as a function of the luminosity, colour coded with $\log \Psi_{\text{dust}}$ for R12 data set. The results for a selected value of $\Psi_{\text{dust}} \approx 800$ are also overplotted. The general trends recovered are analogue for different data sets. For a given luminosity, larger velocities are found at increasing dust content, corresponding to lower values of Ψ_{dust} , as also assumed in equation (18) and predicted by the wind theory. However, for the plotted value of $\Psi_{\text{dust}} = 800$ and for a given luminosity, the scatter of the velocities is up to $\approx 7\text{--}8 \text{ km s}^{-1}$. The predicted spread is expected since other quantities, such as the T_{inn} , T_{eff} and \dot{M} , change among the plotted sources, affecting the velocities (Elitzur & Ivezić 2001; Ivezić & Elitzur 2010). A clear trend between v_{exp} and Ψ_{dust} is highlighted if the variation in Ψ_{dust} spans a large range of values, which is more than one order of magnitude in Fig. 19.

In the upper panel of Fig. 20 we plot the ratios between the velocities obtained with R13 and the value adopted in

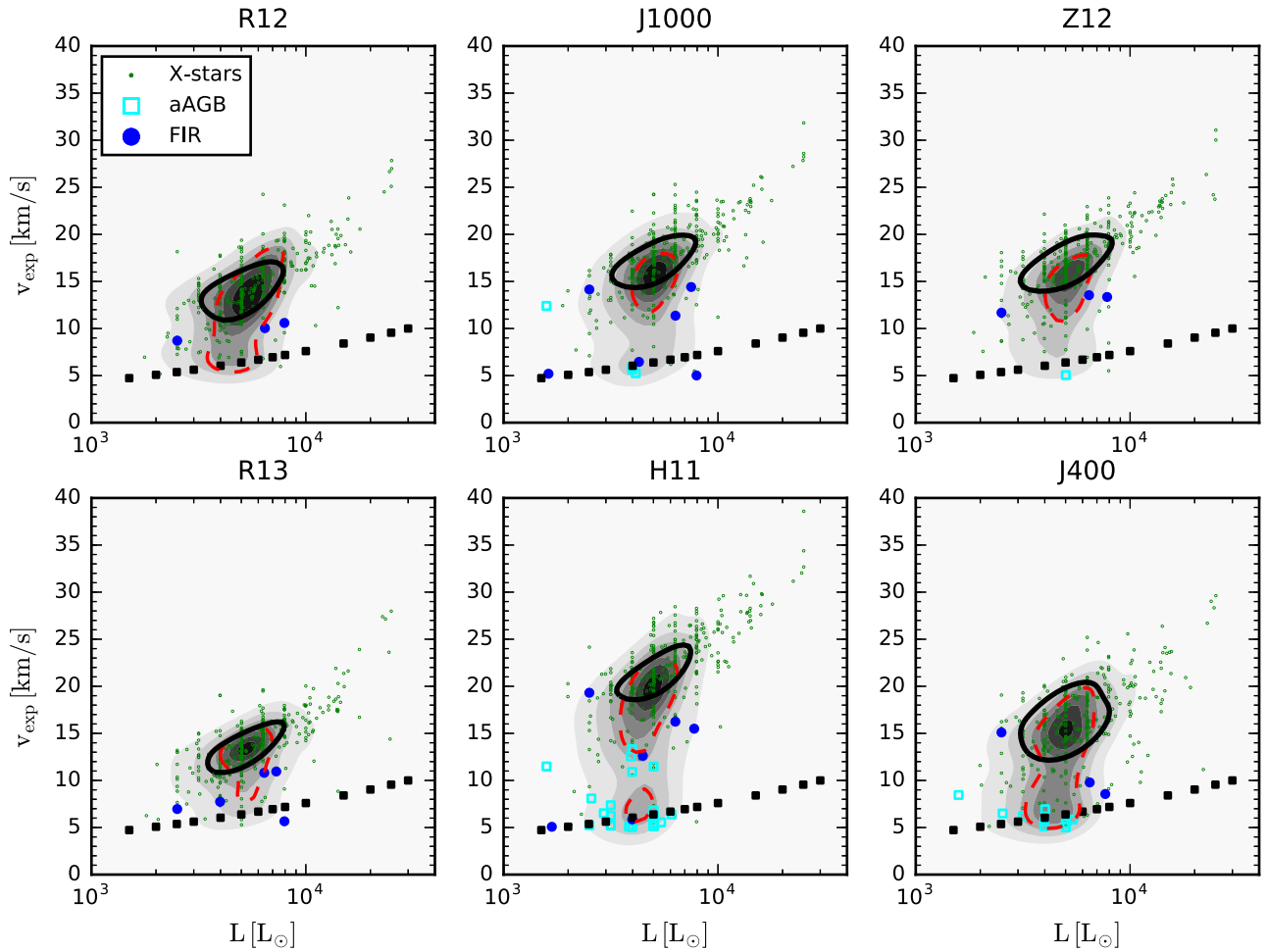


Figure 17. Expansion velocity as a function of the stellar luminosity for all the optical data sets of carbon dust. For comparison, the expansion velocities derived from the scaling relation in equation (18), as in Boyer et al. (2012) and Srinivasan et al. (2016), are also plotted with full black squares (see text for more details). The colour code for the different classes of stars is the same as in Fig. 7.

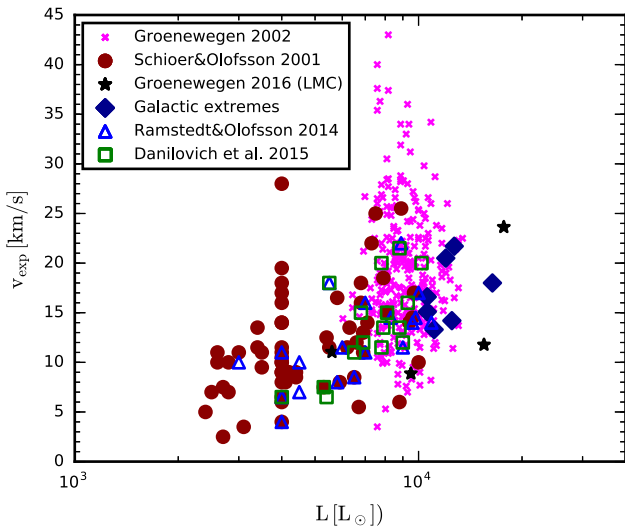


Figure 18. Expansion velocity as a function of the luminosity for the same observations of Galactic and LMC carbon-rich sources shown in Fig. 16.

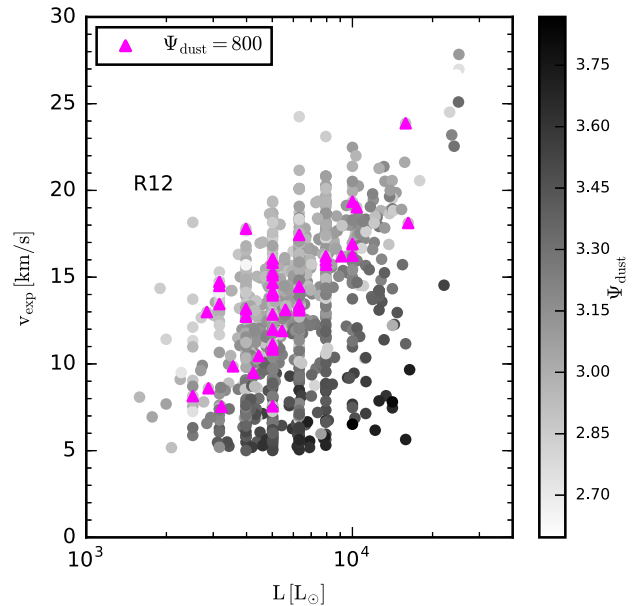


Figure 19. Expansion velocity as a function of luminosity colour coded for the value of Ψ_{dust} derived for R12 data set. The stars with $\Psi_{\text{dust}} \approx 800$ are overplotted (magenta triangles).

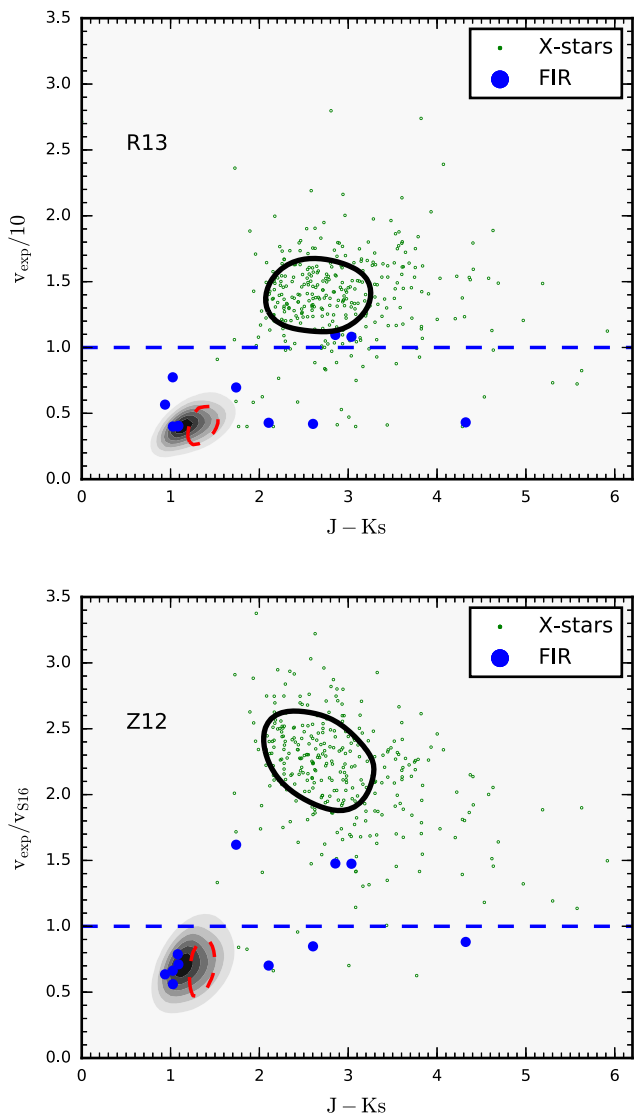


Figure 20. Upper panel: ratio between the velocities obtained from the SED fitting procedure by employing R13 data set, and $v_{\text{exp}} = 10 \text{ km s}^{-1}$, as assumed by Groenewegen et al. (2009), as a function of the $J - K_s$ colour. Lower panel: the same as in the upper panel, but selecting the results for Z12 data set and computing v_{exp} for all the stars by employing the scaling relation in equation (18), as assumed by Boyer et al. (2012) and Srinivasan et al. (2016). The different classes of stars are plotted with the same colour code as in Fig. 7.

Groenewegen et al. (2009) as a function of $J - K_s$. We select for the comparison our R13 data set, since Groenewegen et al. (2009) adopted Rouleau & Martin (1991) in their calculations, assuming that all grains have size of $a \approx 0.1 \mu\text{m}$. The optical properties in Groenewegen et al. (2009) are calculated for a continuous distribution of hollow spheres and not for simple spherical grains (Mie theory). The velocities we predict for the least dust-rich stars are typically less than one half of the assumed value of 10 km s^{-1} . For these stars the dust-driven wind is expected to be inefficient with R13. On the other hand, the typical velocities of the dustiest stars are between ≈ 1.1 and 1.7 times larger than the assumed ones.

In the lower panel of Fig. 20, the expansion velocities obtained for Z12 are compared with the one assumed by Srinivasan et al. (2016) who adopted the ACAR data set by Zubko et al. (1996) with typical spherical grain size of $a \approx 0.1 \mu\text{m}$. Similarly to the upper

plot, the bulk of the dust-poor stars is not efficiently accelerated and shows velocities lower than the assumed ones. On the other hand, the predicted velocities of the most dust-rich sources are between ≈ 1.9 and 2.7 times larger than the assumed ones.

3.3.7 Carbon excess

On the basis of the analysis presented we do not find a clear trend between the value of the carbon excess and $J - K_s$. This can be explained by the small dependence usually found between τ_1 and the carbon excess compared to other stellar parameters, as the mass-loss rate, as shown in the Section 3.1. As a consequence, the carbon excess is not well constrained and the values considered in our grids are almost equally probable for the majority of the sources for all the data sets considered. Different combinations of the mass-loss rates and carbon excess produce a valid fit of the selected source. In particular, for larger values of the mass-loss rate, the corresponding carbon excess increases, whilst for lower values of the mass-loss rate the carbon excess decreases. Such a result suggests that there is a degeneracy between the mass-loss rate and the carbon excess.

3.3.8 Current stellar mass

As well known, the current stellar mass has a minor effect on the emerging stellar spectra. For this reason, we are unable to constrain the current stellar mass by our analysis similarly to what we find for the carbon excess. A better constrain on the current stellar mass might be provided from independent observational determination of the expansion velocities and mass-loss rates of carbon stars in the SMC.

3.4 Dust production rates

We here discuss the DPRs derived for the different optical data sets selected for carbon dust. Our DPRs are shown for the various dust species formed (amC, SiC and iron) and for the different classes of stars, photometrically classified. For aAGBs, we report only half of the DPRs derived from the fitted sources, since about half of the aAGBs are carbon rich (Boyer et al. 2015). Our DPRs are compared with the ones found in the literature.

3.4.1 DPRs for the different dust species

The DPRs for the different dust species and optical data sets for carbon dust are listed in Table 5. For all the optical data sets, the total amount of dust produced is dominated by carbon dust for all the type of stars. The amount of iron dust is low and very uncertain. The smallest uncertainty in the iron dust production is found for the most dust-poor stars and it is between ≈ 50 and 72 per cent depending on the optical data set. The total amount of SiC condensed is as well rather uncertain for the most dust-poor stars. The lowest uncertainties are between ≈ 33 and ≈ 56 per cent, depending on the data set, for X-stars and FIR. The large uncertainties affecting the amount of SiC and iron dust is not surprising since these dust species are affecting the SED of carbon-rich stars less than carbon dust. Moreover, as discussed in Section 3.3.3, a larger uncertainty in the gas-to-dust ratio is expected for the least dusty stars, for which we expect a larger degeneracy in the parameters producing a spectrum that is almost dust-free.

Most of the SiC is produced in CSEs of X-stars. The total amount of SiC can vary up to a factor of ≈ 2.7 for the different optical data

Table 5. DPRs in $M_{\odot} \text{ yr}^{-1}$ divided by dust type and stellar classes. The DPRs listed are computed for the different combinations of optical data sets selected.

	Carbon	SiC	Iron
R13			
C-stars	$(5.37 \pm 0.78) \times 10^{-7}$	$(1.13 \pm 0.86) \times 10^{-9}$	$(6.4 \pm 4.2) \times 10^{-11}$
X-stars	$(2.72 \pm 0.82) \times 10^{-6}$	$(1.47 \pm 0.70) \times 10^{-7}$	$(3.1 \pm 3.3) \times 10^{-10}$
aAGB	$(6.8 \pm 3.4) \times 10^{-9}$	$(3.1 \pm 2.6) \times 10^{-11}$	$(4.7 \pm 3.3) \times 10^{-12}$
FIR	$(6.8 \pm 2.9) \times 10^{-8}$	$(4.9 \pm 2.7) \times 10^{-9}$	$(2.3 \pm 2.4) \times 10^{-11}$
Total	$(3.34 \pm 0.93) \times 10^{-6}$	$(1.53 \pm 0.73) \times 10^{-7}$	$(4.0 \pm 4.0) \times 10^{-10}$
Mass fraction	≈ 96 per cent	≈ 4 per cent	–
R12			
C-stars	$(6.7 \pm 1.1) \times 10^{-7}$	$(2.3 \pm 1.5) \times 10^{-9}$	$(1.62 \pm 0.92) \times 10^{-11}$
X-stars	$(2.98 \pm 0.97) \times 10^{-6}$	$(2.03 \pm 0.86) \times 10^{-8}$	$(2.2 \pm 2.5) \times 10^{-9}$
aAGB	$(7.4 \pm 3.7) \times 10^{-9}$	$(4.5 \pm 3.3) \times 10^{-11}$	$(9.3 \pm 5.8) \times 10^{-12}$
FIR	$(6.8 \pm 2.9) \times 10^{-8}$	$(6.3 \pm 2.5) \times 10^{-9}$	$(1.9 \pm 2.1) \times 10^{-10}$
Total	$(3.7 \pm 1.1) \times 10^{-6}$	$(2.12 \pm 0.90) \times 10^{-7}$	$(2.5 \pm 2.8) \times 10^{-9}$
Mass fraction	≈ 95 per cent	≈ 5 per cent	–
J1000			
C-stars	$(2.57 \pm 0.50) \times 10^{-7}$	$(9.0 \pm 6.3) \times 10^{-10}$	$(5.8 \pm 3.4) \times 10^{-11}$
X-stars	$(1.30 \pm 0.37) \times 10^{-6}$	$(9.6 \pm 4.3) \times 10^{-8}$	$(2.1 \pm 1.7) \times 10^{-10}$
aAGB	$(2.4 \pm 1.3) \times 10^{-9}$	$(1.7 \pm 1.3) \times 10^{-11}$	$(4.2 \pm 2.7) \times 10^{-12}$
FIR	$(2.9 \pm 1.2) \times 10^{-8}$	$(2.7 \pm 1.5) \times 10^{-9}$	$(1.22 \pm 0.96) \times 10^{-11}$
Total	$(1.58 \pm 0.44) \times 10^{-6}$	$(1.00 \pm 0.45) \times 10^{-7}$	$(2.8 \pm 2.2) \times 10^{-10}$
Mass fraction	≈ 94 per cent	≈ 6 per cent	–
J400			
C-stars	$(4.9 \pm 1.3) \times 10^{-7}$	$(1.5 \pm 1.3) \times 10^{-9}$	$(6.5 \pm 4.6) \times 10^{-11}$
X-stars	$(3.2 \pm 1.1) \times 10^{-6}$	$(2.6 \pm 1.0) \times 10^{-7}$	$(4.3 \pm 4.4) \times 10^{-9}$
aAGB	$(4.5 \pm 2.8) \times 10^{-9}$	$(1.8 \pm 1.5) \times 10^{-11}$	$(4.8 \pm 3.2) \times 10^{-12}$
FIR	$(7.0 \pm 3.1) \times 10^{-8}$	$(7.2 \pm 2.9) \times 10^{-9}$	$(3.2 \pm 3.3) \times 10^{-10}$
Total	$(3.8 \pm 1.2) \times 10^{-6}$	$(2.7 \pm 1.1) \times 10^{-7}$	$(4.7 \pm 4.8) \times 10^{-9}$
Mass fraction	≈ 93 per cent	≈ 7 per cent	–
Z12			
C-stars	$(3.30 \pm 0.62) \times 10^{-7}$	$(1.0 \pm 0.76) \times 10^{-9}$	$(6.2 \pm 3.9) \times 10^{-11}$
X-stars	$(1.83 \pm 0.54) \times 10^{-6}$	$(1.42 \pm 0.62) \times 10^{-7}$	$(3.9 \pm 3.7) \times 10^{-10}$
aAGB	$(3.3 \pm 1.7) \times 10^{-9}$	$(2.1 \pm 1.6) \times 10^{-11}$	$(5.2 \pm 3.1) \times 10^{-12}$
FIR	$(4.4 \pm 1.7) \times 10^{-8}$	$(4.4 \pm 2.0) \times 10^{-9}$	$(2.9 \pm 2.6) \times 10^{-11}$
Total	$(2.20 \pm 0.63) \times 10^{-6}$	$(1.47 \pm 0.65) \times 10^{-7}$	$(4.8 \pm 4.4) \times 10^{-10}$
Mass fraction	≈ 94 per cent	≈ 6 per cent	–
H11			
C-stars	$(3.49 \pm 0.81) \times 10^{-7}$	$(2.7 \pm 1.5) \times 10^{-9}$	$(1.23 \pm 0.72) \times 10^{-10}$
X-stars	$(1.72 \pm 0.51) \times 10^{-6}$	$(1.65 \pm 0.58) \times 10^{-7}$	$(1.2 \pm 1.1) \times 10^{-9}$
aAGB	$(2.8 \pm 1.5) \times 10^{-9}$	$(2.8 \pm 1.8) \times 10^{-11}$	$(1.0 \pm 0.51) \times 10^{-11}$
FIR	$(3.7 \pm 1.5) \times 10^{-8}$	$(4.2 \pm 1.4) \times 10^{-9}$	$(8.4 \pm 7.5) \times 10^{-11}$
Total	$(2.11 \pm 0.61) \times 10^{-6}$	$(1.72 \pm 0.61) \times 10^{-7}$	$(1.4 \pm 1.3) \times 10^{-9}$
Mass fraction	≈ 92 per cent	≈ 8 per cent	–

sets (see J1000 and J400). The SiC mass fraction over the total is between ≈ 4 and ≈ 8 per cent (see R13 and H11). On the other hand, the total iron dust produced is always negligible.

3.4.2 Contribution of the different classes of stars to the total DPR

In Table 6 the values of the DPRs are shown for the different classes of stars. As far as aAGBs are concerned, we list as final DPR half of the total amount obtained from our analysis, since, as discussed by Boyer et al. (2015), only about half of the aAGBs are expected to be C-rich.

The largest contribution to the total DPR is always provided by X-stars (≈ 82 – 87 per cent) and the remaining DPR is mainly due to C-stars. In fact, aAGBs always yield a very small amount of dust with respect to the total (≈ 0.1 per cent). The DPR of the FIR sources is usually larger than the one of all the aAGB stars, even though the value is rather uncertain. The DPR of FIR is only ≈ 2 per cent of the DPRs of all the other sources. However, the amount of dust produced by the FIR is surprisingly large if compared with the one of aAGBs, since FIR are only 11, while aAGBs are ≈ 550 . The average DPR of FIR is about ≈ 3 – $7 \times 10^{-9} M_{\odot} \text{ yr}^{-1}$, depending on the optical data set. This value is close to the one of X-stars and is typically ≈ 20 times larger than the one of C-star. On the other

Table 6. Total and average DPRs in $M_{\odot} \text{ yr}^{-1}$ computed for the different combinations of optical data sets selected and listed for the different classes of stars. Other DPRs found in the literature are also shown.

	C-stars	X-stars	aAGB	FIR	Total (no FIR)
This work					
Number of stars	1715	339	1092	11	–
R13	$(5.38 \pm 0.79) \times 10^{-7}$	$(2.87 \pm 0.89) \times 10^{-6}$	$(6.9 \pm 3.4) \times 10^{-9}$	$(7.3 \pm 3.2) \times 10^{-8}$	$(3.42 \pm 0.98) \times 10^{-6}$
R12	$(6.7 \pm 1.1) \times 10^{-7}$	$(3.2 \pm 1.1) \times 10^{-6}$	$(7.4 \pm 3.7) \times 10^{-9}$	$(7.4 \pm 3.2) \times 10^{-8}$	$(3.9 \pm 1.2) \times 10^{-6}$
J1000	$(2.57 \pm 0.50) \times 10^{-7}$	$(1.39 \pm 0.42) \times 10^{-6}$	$(2.4 \pm 1.3) \times 10^{-9}$	$(3.2 \pm 1.3) \times 10^{-8}$	$(1.65 \pm 0.47) \times 10^{-6}$
J400	$(5.0 \pm 1.3) \times 10^{-7}$	$(3.5 \pm 1.2) \times 10^{-6}$	$(4.5 \pm 2.8) \times 10^{-9}$	$(7.8 \pm 3.4) \times 10^{-8}$	$(4.0 \pm 1.3) \times 10^{-6}$
Z12	$(3.31 \pm 0.63) \times 10^{-7}$	$(1.97 \pm 0.61) \times 10^{-6}$	$(3.3 \pm 1.7) \times 10^{-9}$	$(4.9 \pm 1.9) \times 10^{-8}$	$(2.30 \pm 0.67) \times 10^{-6}$
H11	$(3.52 \pm 0.82) \times 10^{-7}$	$(1.89 \pm 0.57) \times 10^{-6}$	$(2.8 \pm 1.5) \times 10^{-9}$	$(4.2 \pm 1.6) \times 10^{-8}$	$(2.24 \pm 0.66) \times 10^{-6}$
Srinivasan et al. (2016)					
Number of stars	1652	337	–	–	–
	$\approx 1.2 \times 10^{-7}$	$\approx 6.8 \times 10^{-7}$	–	–	$\approx 8.0 \times 10^{-7}$
Boyer et al. (2012)					
Number of stars	1559	313	–	–	–
	$\approx 1.2 \times 10^{-7}$	$\approx 6.3 \times 10^{-7}$	–	–	$\approx 7.5 \times 10^{-7}$
Matsuura et al. (2013)					
	–	–	–	–	$\approx 4 \times 10^{-6}$

hand, the average DPR of aAGBs is typically $\approx 10^{-11} M_{\odot} \text{ yr}^{-1}$ or less.

3.4.3 Total DPRs for the different optical data sets and compared with the literature

The total DPRs obtained for different optical data sets are shown in Table 6 together with other results found in the literature. Depending on the optical data set, we find that the first ~ 250 most dust-producing stars provide the ≈ 80 per cent of the total DPR. The two most extreme values of the DPRs are obtained for J1000 ($\approx 1.65 \times 10^{-6} M_{\odot} \text{ yr}^{-1}$) and J400 ($\approx 4.0 \times 10^{-6} M_{\odot} \text{ yr}^{-1}$), respectively. The variation between these two values is of a factor of ≈ 2.4 .

For all the optical data sets, the typical uncertainty of the total dust production is around ≈ 30 per cent. Since the uncertainties were estimated by analysing the variation of the photometry due to a random variation within the photometric error, we conclude that the precision of the photometry allows for a determination of the total DPR that is typically no better than ≈ 30 per cent. Within the estimated uncertainties, the DPRs for the different data sets are compatible except for the one computed with J1000.

We compare the results of our investigations with others in the literature. In the works by Boyer et al. (2012) and Srinivasan et al. (2016) the optical data set adopted for the SED fitting procedure is the ACAR sample by Zubko et al. (1996). Differently from our approach, a grain size distribution is assumed, with a typical grain size of $a \approx 0.1 \mu\text{m}$. The grains are also assumed to be spherical. The most natural comparison between Boyer et al. (2012), Srinivasan et al. (2016) and our work is with Z12 (see Table 1). Our DPRs can only be compared with the DPRs of Boyer et al. (2012) and Srinivasan et al. (2016) computed for C- and X-stars. In fact, in Boyer et al. (2012) and Srinivasan et al. (2016) a fraction of aAGBs and FIR sources are treated as O-rich and the DPR is computed for the complete sample including C- and O-rich stars. For this reason, the value of the DPRs of aAGBs and FIR for Boyer et al. (2012) and Srinivasan et al. (2016) is not listed in Table 6.

From Table 6 we can appreciate that the DPRs computed by Boyer et al. (2012) and Srinivasan et al. (2016) are ≈ 3 times lower than Z12 for both C- and X-stars. The average DPRs computed for Z12 are also in line with this result. By employing Z12, our average DPR for C-stars is $\approx 1.9 \times 10^{-10} M_{\odot} \text{ yr}^{-1}$, to be compared with Boyer

et al. (2012), $\approx 7.8 \times 10^{-11} M_{\odot} \text{ yr}^{-1}$, and with Srinivasan et al. (2016), $\approx 7.1 \times 10^{-11} M_{\odot} \text{ yr}^{-1}$. On the other hand, the average DPR of X-stars with Z12 is $\approx 5.8 \times 10^{-9} M_{\odot} \text{ yr}^{-1}$, which is again almost three times larger than the one derived by Boyer et al. (2012) and Srinivasan et al. (2016), $\approx 2.0 \times 10^{-9} M_{\odot} \text{ yr}^{-1}$. Furthermore, the DPRs of Boyer et al. (2012) and Srinivasan et al. (2016) are about ≈ 5 times lower than the largest DPR obtained employing our grid of models (J400). Our lowest DPR, obtained with J1000, is still a factor of ≈ 2 larger than the ones estimated by Boyer et al. (2012) and Srinivasan et al. (2016).

The differences between our DPRs and the ones derived by Boyer et al. (2012) and Srinivasan et al. (2016) for comparable dust opacities are dependent on several factors. First of all, as shown in Fig. 17 and in the lower panel of Fig. 20 there are considerable differences in the expansion velocities, up to a factor of 3 for the most dust-enshrouded X-stars. The final velocity affects the estimate of the dust mass-loss rate as can be seen from equation (17). The possible differences arising as consequence of different assumptions on the expansion velocity, were already pointed out by Srinivasan et al. (2016) when comparing their results with the ones by Matsuura et al. (2013). In addition to that, we do not expect to obtain the same condensation radius, R_c , from our model and from the fitting procedure by Srinivasan et al. (2016). Moreover, as shown in Section 3.3.5 carbon stars fitted with our models can yield grain size quite different from the standard assumption of $0.1 \mu\text{m}$, which also affects the absorption, scattering and extinction properties of dust grains.

On the other hand, Matsuura et al. (2013) estimated the total DPR for carbon-rich stars basing their analysis on the work by Groenewegen et al. (2009). In Groenewegen et al. (2009), the optical data set selected for carbon dust is the one by Rouleau & Martin (1991). A single value of the grain size of $0.1 \mu\text{m}$ is also adopted. In Groenewegen et al. (2009) the optical properties of dust grains are not calculated for spherical grains, but for a continuous distribution of hollow spheres. This choice accounts more consistently for the possible porosity of dust grains, which is not taken into account assuming spherical grains. The most natural choice is then to compare the total DPR derived by Matsuura et al. (2013) with R13, even though we employ spherical grains, for which the optical properties are calculated with the Mie theory. The total DPR estimated by Matsuura et al. (2013) is in fair agreement with both R13 and R12 within the uncertainty. The DPR of Matsuura et al. (2013) is

however ≈ 2.4 times larger than the lowest value predicted by our analysis (J1000). Furthermore, we never obtain a DPR larger than the one of Matsuura et al. (2013) for any of the data sets considered.

4 SUMMARY AND CONCLUSIONS

In this work we provide physically grounded dusty models and spectra suitable to fit the photometry of the C-rich TP-AGB stars of the SMC. We perform such an investigation for some selected choices of optical data sets for carbon dust and seed particle abundances that have been shown to well reproduce simultaneously most of the CCDs in the SMC (Nanni et al. 2016). From the SED fitting procedure we are able to consistently derive some important dust properties and stellar quantities, such as bolometric luminosities, mass-loss rates, gas-to-dust ratios, outflow expansion velocities and the dust grain sizes. These results may be helpfully employed to test the predictions of stellar evolution models (Marigo et al. 2013, 2016) and synthetic stellar populations including AGB stars (Marigo et al. 2017).

We here summarize the main results.

(i) *Luminosities.* We find that the luminosities are well constrained by the SED fitting procedure. Our luminosity function is in excellent agreement with the one derived by Srinivasan et al. (2016). The position of the peak is around $M_{\text{bol}} \approx -4.5$, in good agreement with the results obtained from the catalogue by Rebeiro et al. (1993).

(ii) *Mass-loss rates.* C- and X-stars are separated in term of mass-loss rates around $\log \dot{M} \approx -6$, which correspond to $J - K_s \approx 2$. Anomalous AGBs are always characterized by $\log \dot{M} \lesssim -6$ for all the data sets considered. The mass-loss rates can vary up to a factor of ≈ 2 for different optical data sets for the most dust-enshrouded X-stars and up to a factor of ≈ 7 – 8 for C-stars, in the most extreme cases. Our distribution of mass-loss rates for X-stars is similar in terms of shape to the one derived from the observations of dust-enshrouded Galactic stars by Groenewegen et al. (2002), especially for R13 and J400 data sets. However, the position of the peak is shifted to lower mass-loss rates for our distributions. On the other hand, the distribution of C-stars is compared to the one derived from the Galactic observations by Schöier & Olofsson (2001), for a sample of optically bright carbon stars. Our distributions are more peaked than the one of optically bright carbon stars with the peak shifted to larger values of the mass-loss rate.

(iii) *Gas-to-dust ratios.* The majority of X-stars have gas-to-dust ratios lower than C-stars. The value of Ψ_{dust} is never as low as the value usually adopted in the literature ($\Psi_{\text{dust}} = 200$). The range of possible values of Ψ_{dust} is quite large, with $500 \lesssim \Psi_{\text{dust}} \lesssim 800$ – 2000 for X-stars, and $\Psi_{\text{dust}} \gtrsim 800$ – 2000 for C-stars. The large values of Ψ_{dust} for aAGBs are consistent with a low amount of dust in the CSEs of these stars, in agreement with Boyer et al. (2011). C- and X-stars are separated around $\Psi_{\text{dust}} \approx 800$ – 2000 , depending on the optical data set for carbon dust. The gas-to-dust ratio obtained with different optical constants can vary up to a factor of ≈ 1.4 – 1.9 for the dustiest stars, and up to ≈ 7 , in the most extreme cases, for dust-poor sources.

The large range of possible values of Ψ_{dust} suggests that the choice of a unique value for Ψ_{dust} , as usually assumed, might not in general be suitable for all the C-rich stars, as also noticed by Eriksson et al. (2014).

The gas-to-dust ratio anticorrelates with the mass-loss rates. Such a trend suggests that the dust condensation efficiency increases with the density in the CSEs. The relation between Ψ_{dust} and \dot{M} is very

steep for $\log \dot{M} \lesssim -6$ and it tends to saturate for $\log \dot{M} \gtrsim -6$. Indeed, for mass-loss rates larger than this threshold value, the dependence between Ψ_{dust} and \dot{M} is milder.

(iv) *Grain sizes.* For all the carbon dust optical data sets considered, larger grain sizes are predicted for redder stars. The most important parameter affecting the final grain size is the seed particle abundance. The scaling relation between these two quantities is $a_{\text{amC}} \propto (\epsilon_s)^{-1/3}$, as roughly recovered in our analysis.

(v) *Outflow expansion velocity.* The final velocity of the outflow is dependent on the optical data set assumed for carbon dust and on the seed particle abundance. Expansion velocities are expected to increase as a function of the mass-loss rate and of the luminosity. Above a certain value of \dot{M} , which depends on the set of optical constants, the outflow is accelerated. For \dot{M} above this threshold, the velocity increases with the mass-loss rate, attaining its maximum value around $-5.7 \lesssim \dot{M} \lesssim -5.6$. Typical values of the maximum velocity attained are in the range $20 \lesssim v_{\text{exp}} \lesssim 25 \text{ km s}^{-1}$. However, the predicted velocities for the dustiest stars show a large scatter. The velocities of the stars analysed linearly scale with the stellar luminosity and with the gas-to-dust ratio, as predicted by the wind theory. For all the optical data sets, the outflow is accelerated above $L \approx 2000 L_{\odot}$.

The velocities of the dustiest stars are typically ≈ 1.9 – 2.7 times larger than the ones adopted by Boyer et al. (2012) and Srinivasan et al. (2016), and ≈ 1.1 – 1.7 times larger than the value of $v_{\text{exp}} = 10 \text{ km s}^{-1}$, assumed by Groenewegen et al. (2007).

The trends between v_{exp} and \dot{M} and between v_{exp} and L are in general comparable to the ones observed for Galactic stars. This result suggests that the dynamical properties of the outflow for carbon stars are rather independent of the metallicity. Such a trend is in agreement with the predictions of hydrodynamical calculations according to which the critical parameter determining the outflow expansion velocity is the carbon excess, rather than the metallicity (Mattsson et al. 2010; Eriksson et al. 2014).

(vi) *Other stellar quantities.* Input stellar quantities such as the carbon excess and the current stellar mass are not constrained by our analysis. Some degeneracy is expected among some of our models.

From the SED fitting analysis we compute the DPRs of the selected stars for the different optical data sets selected. We compare the results with the ones of the literature. The main results are summarized below.

(i) The bulk of the dust produced is made of solid carbon for all the classes of stars. The amount of SiC dust can be up to ≈ 8 per cent of the total. The amount of metallic iron produced is always negligible.

(ii) The total DPR is dominated by X-stars for which the contribution to the dust budget in mass is ≈ 85 per cent. The DPRs obtained for different optical data sets of carbon dust are comparable within the estimated uncertainties, except for J1000 data set for which the DPR is lower. The variation of the total DPR computed with different optical constants is up to a factor of ≈ 2.4 .

(iii) Our DPR is in good agreement with the one derived by Matsuura et al. (2013) for comparable optical constants of carbon dust. However, the DPR estimated by these authors can be up to a factor of ≈ 2.4 times larger than the one derived by our analysis (see J1000). On the other hand, none among our data sets yield a DPR larger than the one by Matsuura et al. (2013).

The DPRs of Boyer et al. (2012) and Srinivasan et al. (2016) are ≈ 3 times lower than the one we obtain for comparable optical constants of carbon dust. Moreover, the largest and the lowest DPRs

predicted by our analysis are, respectively, ≈ 5 and ≈ 2 times larger than the ones by these authors. The difference found with these works for similar optical data sets can be due to several factors. For example, the predicted expansion velocities of our models are larger than the ones they adopted. Part of the discrepancy could also be ascribed to the assumptions related to the grain size distributions and to differences in the condensation radii and dust temperatures.

Our grids of models including the spectra and other relevant dust and stellar quantities are publicly available at <http://starkey.astro.unipd.it/web/guest/dustymodels>.

ACKNOWLEDGEMENTS

This work is supported by the ERC Consolidator Grant funding scheme (project STARKEY, G.A. no. 615604).

REFERENCES

- Andersen A. C., Loidl R., Höfner S., 1999, *A&A*, 349, 243
 Aringer B., Girardi L., Nowotny W., Marigo P., Bressan A., 2016, *MNRAS*, 457, 3611
 Blum R. D. et al., 2006, *AJ*, 132, 2034
 Bohren C. F., Huffman D. R., Kam Z., 1983, *Nature*, 306, 625
 Bolatto A. D. et al., 2007, *ApJ*, 655, 212
 Boyer M. L. et al., 2011, *AJ*, 142, 103
 Boyer M. L. et al., 2012, *ApJ*, 748, 40
 Boyer M. L. et al., 2013, *ApJ*, 774, 83
 Boyer M. L., McDonald I., Srinivasan S., Zijlstra A., van Loon J. T., Olsen K. A. G., Sonneborn G., 2015, *ApJ*, 810, 116
 Bressan A., Granato G. L., Silva L., 1998, *A&A*, 332, 135
 Cherchneff I., Barker J. R., Tielens A. G. G. M., 1992, *ApJ*, 401, 269
 Cioni M.-R. L., Girardi L., Marigo P., Habing H. J., 2006, *A&A*, 448, 77
 Danilovich T. et al., 2015, *A&A*, 581, A60
 de Grijs R., Bono G., 2015, *AJ*, 149, 179
 Dell’Agli F., Ventura P., Schneider R., Di Criscienzo M., García-Hernández D. A., Rossi C., Brocato E., 2015a, *MNRAS*, 447, 2992
 Dell’Agli F., García-Hernández D. A., Ventura P., Schneider R., Di Criscienzo M., Rossi C., 2015b, *MNRAS*, 454, 4235
 Elitzur M., Ivezić Ž., 2001, *MNRAS*, 327, 403
 Eriksson K., Nowotny W., Höfner S., Aringer B., Wachter A., 2014, *A&A*, 566, A95
 Ferrarotti A. S., Gail H.-P., 2006, *A&A*, 447, 553
 Goldman S. R. et al., 2017, *MNRAS*, 465, 403
 Gordon K. D. et al., 2011, *AJ*, 142, 102
 Groenewegen M. A. T., 2006, *A&A*, 448, 181
 Groenewegen M. A. T., 2012, *A&A*, 543, A36
 Groenewegen M. A. T., Sevenster M., Spoon H. W. W., Pérez I., 2002, *A&A*, 390, 501
 Groenewegen M. A. T. et al., 2007, *MNRAS*, 376, 313
 Groenewegen M. A. T., Sloan G. C., Soszyński I., Petersen E. A., 2009, *A&A*, 506, 1277
 Groenewegen M. A. T. et al., 2016, *A&A*, 596, A50
 Gullieuszik M. et al., 2012, *A&A*, 537, A105
 Habing H. J., Tignon J., Tielens A. G. G. M., 1994, *A&A*, 286, 523
 Hanner M., 1988, Grain Optical Properties. Technical Report
 Ita Y. et al., 2010, *PASJ*, 62, 273
 Ivezić Z., Elitzur M., 1997, *MNRAS*, 287, 799
 Ivezić Ž., Elitzur M., 2010, *MNRAS*, 404, 1415
 Jager C., Mutschke H., Henning T., 1998, *A&A*, 332, 291
 Kato D. et al., 2007, *PASJ*, 59, 615
 Kim S.-H., Martin P. G., Hendry P. D., 1994, *ApJ*, 422, 164
 Leksina I., Penkina N., 1967, *Fizik. Metall. Metalloved.*, 23, 344
 Lewis I. J. et al., 2002, *MNRAS*, 333, 279
 Marigo P., Girardi L., Bressan A., Groenewegen M. A. T., Silva L., Granato G. L., 2008, *A&A*, 482, 883
 Marigo P., Bressan A., Nanni A., Girardi L., Pumo M. L., 2013, *MNRAS*, 434, 488
 Marigo P., Ripamonti E., Nanni A., Bressan A., Girardi L., 2016, *MNRAS*, 456, 23
 Marigo P. et al., 2017, *ApJ*, 835, 77
 Matsuura M. et al., 2005, *A&A*, 434, 691
 Matsuura M. et al., 2009, *MNRAS*, 396, 918
 Matsuura M., Woods P. M., Owen P. J., 2013, *MNRAS*, 429, 2527
 Mattsson L., Wahlin R., Höfner S., 2010, *A&A*, 509, A14
 Nanni A., Bressan A., Marigo P., Girardi L., 2013, *MNRAS*, 434, 2390
 Nanni A., Bressan A., Marigo P., Girardi L., 2014, *MNRAS*, 438, 2328
 Nanni A., Marigo P., Groenewegen M. A. T., Aringer B., Girardi L., Pastorelli G., Bressan A., Bladh S., 2016, *MNRAS*, 462, 1215
 Palmer L. G., Wing R. F., 1982, *AJ*, 87, 1739
 Pegourie B., 1988, *A&A*, 194, 335
 Ramstedt S., Olofsson H., 2014, *A&A*, 566, A145
 Rebeiro E., Azzopardi M., Westerlund B. E., 1993, *A&AS*, 97, 603
 Riebel D., Srinivasan S., Sargent B., Meixner M., 2012, *ApJ*, 753, 71
 Rouleau F., Martin P. G., 1991, *ApJ*, 377, 526
 Ruffle P. M. E. et al., 2015, *MNRAS*, 451, 3504
 Saunders W. et al., 2004, in Moorwood A. F. M., Iye M., eds, *Proc. SPIE*, Vol. 5492, Ground-Based Instrumentation for Astronomy. SPIE, Bellingham, p. 389
 Schöier F. L., Olofsson H., 2001, *A&A*, 368, 969
 Sharp R. et al., 2006, *Proc. SPIE*, 6269, 62690G
 Skrutskie M. F. et al., 2006, *AJ*, 131, 1163
 Srinivasan S., Sargent B. A., Meixner M., 2011, *A&A*, 532, A54
 Srinivasan S., Boyer M. L., Kemper F., Meixner M., Sargent B. A., Riebel D., 2016, *MNRAS*, 457, 2814
 Udalski A., Szymanski M. K., Soszynski I., Poleski R., 2008, *Acta Astron.*, 58, 69
 van Loon J. T., 2006, in Lamers H. J. G. L. M., Langer N., Nugis T., Annuk K., eds, *ASP Conf. Ser. Vol. 353, Stellar Evolution at Low Metallicity: Mass Loss, Explosions, Cosmology*. Astron. Soc. Pac., San Francisco, p. 211
 van Loon J. T., Zijlstra A. A., Whitelock P. A., Waters L. B. F. M., Loup C., Trams N. R., 1997, *A&A*, 325, 585
 van Loon J. T., McDonald I., Oliveira J. M., Evans A., Boyer M. L., Gehrz R. D., Polonski E., Woodward C. E., 2006, *A&A*, 450, 339
 van Loon J. T., Cohen M., Oliveira J. M., Matsuura M., McDonald I., Sloan G. C., Wood P. R., Zijlstra A. A., 2008, *A&A*, 487, 1055
 Ventura P. et al., 2012, *MNRAS*, 424, 2345
 Ventura P., Dell’Agli F., Schneider R., Di Criscienzo M., Rossi C., La Franca F., Gallerani S., Valiante R., 2014, *MNRAS*, 439, 977
 Ventura P., Karakas A. I., Dell’Agli F., García-Hernández D. A., Boyer M. L., Di Criscienzo M., 2016, *MNRAS*, 457, 1456
 Westerlund B. E., Azzopardi M., Breysacher J., 1986, *A&AS*, 65, 79
 Zaritsky D., Harris J., Thompson I. B., Grebel E. K., Massey P., 2002, *AJ*, 123, 855
 Zubko V. G., Mennella V., Colangeli L., Bussoletti E., 1996, *MNRAS*, 282, 1321

APPENDIX A: PHOTOMETRY SELECTION

We here discuss how the observed photometry is selected to perform the SED fitting.

We visually inspected the SED of C-rich stars in the catalogue, finding that in some cases the photometric points of the optical bands (*UBVI*), and, more rarely, of some bands in the NIR cannot be associated with the SED of an AGB star. Some examples in which the optical photometry is at odd with the NIR bands, one is shown in Fig. A1. The disagreement found between the optical and NIR photometry can be due to a mismatch of the sources in different catalogue or to the presence of a binary system. The observed photometry in the visual bands that are not in agreement with the NIR bands has been removed from our fitting procedure. For one particular source (SSTISAGEMA J011219.72–735125.9), plotted in the upper panel of Fig. A1, we also exclude the *J* and *H*

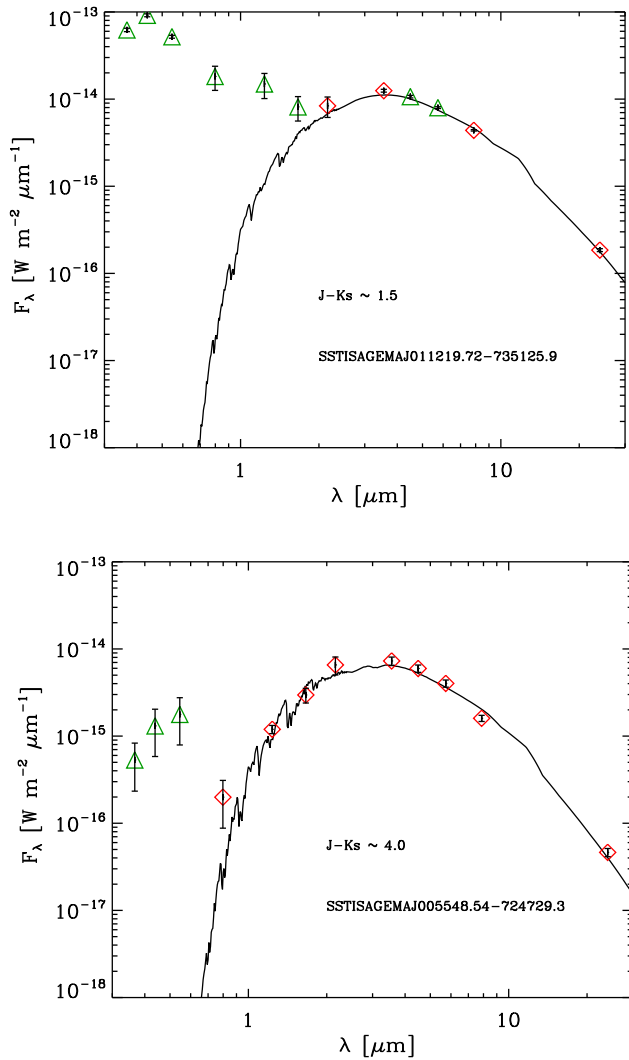


Figure A1. Two examples of sources for which the optical photometric data points are not in agreement with the NIR ones. The observed photometric points, taken from the catalogue by Srinivasan et al. (2016), are plotted with red diamonds, if the points are included in the fit, and with green triangles, if they are excluded. The uncertainty bars are also overplotted. The best-fitting spectra among our grid of models are overplotted with a black solid line for each of the sources.

bands from the SED fitting procedure. The list of sources for which some of the optical bands have been excluded from the SED fitting procedure is listed in Table A1.

The photometry for the *Akari* S11, L15 and *WISE* W3 is available for a sample of 117 sources in the catalogue by Srinivasan et al. (2016). For W3 a systematic offset towards fluxes lower than L15, which is around the same wavelength, is found by Srinivasan et al. (2016). In Fig. A2 we show the fluxes obtained from the photometry listed in Srinivasan et al. (2016) (red diamonds) overplotted with the IRS spectra (black crosses) and with the corresponding fluxes convolved with the S11 and L15 filters (black triangles). For comparison, we also plot the flux of the *Akari* bands obtained from the photometry in the catalogue by Ita et al. (2010), indicated with blue asterisks. For the stars shown, Ita et al. (2010) only contain data in the S11 filter. From the two panels we notice that there is inconsistency between the photometry listed in Srinivasan et al. (2016) and Ita et al. (2010). For the reasons discussed above, we exclude

Table A1. Optical/NIR photometry excluded for the SED fitting.

Name	Optical/NIR bands excluded
SSTSAGEMA J002124.62–734450.1	<i>VI</i>
SSTSAGEMA J002358.52–733754.9	<i>I</i>
SSTSAGEMA J002942.24–731911.1	<i>U</i>
SSTSAGEMA J003040.75–734245.1	<i>BV</i>
SSTSAGEMA J003117.69–722726.0	<i>U</i>
SSTSAGEMA J003314.99–740211.7	<i>U</i>
SSTSAGEMA J003346.13–724458.5	<i>BV</i>
SSTSAGEMA J003639.49–721626.6	<i>BV</i>
SSTSAGEMA J003905.71–724716.3	<i>B</i>
SSTSAGEMA J004116.96–725216.6	<i>U</i>
SSTSAGEMA J004125.96–735345.6	<i>U</i>
SSTSAGEMA J004210.64–735003.6	<i>B</i>
SSTSAGEMA J004221.80–722405.8	<i>UBV</i>
SSTSAGEMA J004305.88–732140.7	<i>V</i>
SSTSAGEMA J004308.75–734825.2	<i>B</i>
SSTSAGEMA J004325.20–721851.0	<i>BV</i>
SSTSAGEMA J004333.05–724803.7	<i>U</i>
SSTSAGEMA J004339.55–731457.6	<i>UB</i>
SSTSAGEMA J004346.41–733828.0	<i>B</i>
SSTSAGEMA J004353.49–724854.5	<i>BVI</i>
SSTSAGEMA J004442.81–725914.6	<i>UB</i>
SSTSAGEMA J004453.12–721606.0	<i>B</i>
SSTSAGEMA J004457.03–730556.0	<i>U</i>
SSTSAGEMA J004502.13–725224.2	<i>BV</i>
SSTSAGEMA J004516.87–734133.4	<i>U</i>
SSTSAGEMA J004641.37–730613.5	<i>UBVIJ</i>
SSTSAGEMA J004648.02–731709.4	<i>B</i>
SSTSAGEMA J004657.56–723224.8	<i>U</i>
SSTSAGEMA J004720.41–722503.7	<i>U</i>
SSTSAGEMA J004756.89–722614.5	<i>U</i>
SSTSAGEMA J004805.77–731743.5	<i>BVI</i>
SSTSAGEMA J004825.72–724402.8	<i>VI</i>
SSTSAGEMA J004903.78–730520.1	<i>B</i>
SSTSAGEMA J004916.97–732229.0	<i>UB</i>
SSTSAGEMA J004922.69–731454.5	<i>U</i>
SSTSAGEMA J004931.48–730715.9	<i>B</i>
SSTSAGEMA J004941.35–731623.8	<i>UB</i>
SSTSAGEMA J004942.70–730220.8	<i>BV</i>
SSTSAGEMA J004949.95–724514.4	<i>VI</i>
SSTSAGEMA J004956.41–725933.4	<i>UB</i>
SSTSAGEMA J005012.17–725319.0	<i>UB</i>
SSTSAGEMA J005013.29–731113.1	<i>UB</i>
SSTSAGEMA J005015.26–731243.8	<i>UB</i>
SSTSAGEMA J005016.63–732517.7	<i>B</i>
SSTSAGEMA J005022.85–732249.7	<i>UB</i>
SSTSAGEMA J005031.30–722913.0	<i>B</i>
SSTSAGEMA J005045.34–731839.6	<i>U</i>
SSTSAGEMA J005052.64–725216.5	<i>BV</i>
SSTSAGEMA J005057.36–730106.1	<i>UB</i>
SSTSAGEMA J005102.05–725925.6	<i>B</i>
SSTSAGEMA J005105.61–733625.0	<i>BVI</i>
SSTSAGEMA J005109.24–731933.3	<i>B</i>
SSTSAGEMA J005145.14–732033.7	<i>UB</i>
SSTSAGEMA J005145.18–731805.3	<i>U</i>
SSTSAGEMA J005148.79–730243.8	<i>UB</i>
SSTSAGEMA J005207.42–732138.2	<i>UB</i>
SSTSAGEMA J005222.67–721846.0	<i>U</i>
SSTSAGEMA J005224.60–721115.2	<i>UB</i>
SSTSAGEMA J005229.78–734657.3	<i>U</i>
SSTSAGEMA J005233.39–725409.8	<i>UB</i>
SSTSAGEMA J005259.03–722811.2	<i>UB</i>
SSTSAGEMA J005313.98–731517.4	<i>U</i>
SSTSAGEMA J005315.62–731212.9	<i>U</i>
SSTSAGEMA J005354.59–732204.0	<i>BVI</i>

Table A1 – continued

Name	Optical/NIR bands excluded
SSTISAGEMA J005356.22–703804.1	U B V I
SSTISAGEMA J005357.32–733433.0	B
SSTISAGEMA J005407.65–723628.7	U B
SSTISAGEMA J005408.52–721420.4	B
SSTISAGEMA J005421.12–731544.3	B
SSTISAGEMA J005422.26–724329.8	VI
SSTISAGEMA J005433.07–725814.2	B
SSTISAGEMA J005509.96–734244.7	B
SSTISAGEMA J005514.27–732505.3	U B V I
SSTISAGEMA J005526.63–724514.3	U
SSTISAGEMA J005528.97–724848.6	U B
SSTISAGEMA J005533.34–724127.1	B
SSTISAGEMA J005548.54–724729.3	U B V
SSTISAGEMA J005625.52–740047.0	B V
SSTISAGEMA J005656.43–733530.1	B V
SSTISAGEMA J005705.82–741316.5	U
SSTISAGEMA J005710.93–723100.1	U B V
SSTISAGEMA J005727.64–725327.9	U B V
SSTISAGEMA J005749.03–730521.5	U B
SSTISAGEMA J005858.17–723911.5	U
SSTISAGEMA J005936.59–722717.0	U
SSTISAGEMA J005942.96–730443.2	U B
SSTISAGEMA J005958.80–720300.9	B
SSTISAGEMA J010015.66–722226.1	U
SSTISAGEMA J010053.23–722333.6	U
SSTISAGEMA J010149.32–724900.0	U
SSTISAGEMA J010218.12–722820.8	U
SSTISAGEMA J010245.16–741257.4	U B V I
SSTISAGEMA J010307.18–720629.5	B V I J
SSTISAGEMA J010441.50–712609.9	I
SSTISAGEMA J010442.35–730142.8	U
SSTISAGEMA J010503.13–715929.7	U B V I J H
SSTISAGEMA J010552.88–721902.4	U
SSTISAGEMA J010555.92–723244.0	U B
SSTISAGEMA J010615.16–721653.1	U
SSTISAGEMA J010752.86–714617.1	B
SSTISAGEMA J010810.35–725307.9	B
SSTISAGEMA J010812.96–725243.9	U B V
SSTISAGEMA J010820.66–725252.0	U B
SSTISAGEMA J010858.23–724142.1	B
SSTISAGEMA J010901.19–732015.3	U
SSTISAGEMA J010928.94–722821.2	B
SSTISAGEMA J011032.24–730504.0	B V
SSTISAGEMA J011219.65–724108.4	VI
SSTISAGEMA J011219.72–735125.9	U B V I J H
SSTISAGEMA J011642.41–722725.7	U

from the SED fitting procedure the *Akari* S11, L15 and the *WISE* W3 fluxes. The exclusion of these photometric points is expected to produce only a minor effect on the results of the SED fitting.

For the MIR bands we consider in the fit the IRAC photometry at 4.5 and 5.8 μm only for dust-enshrouded stars with $J - K_s \geq 2$. In fact, as discussed in Nanni et al. (2016), the 4.5 and 5.8 μm bands of C-stars with a low amount of dust are affected by the C_3 feature, for which the available molecular opacity does not fit the feature.

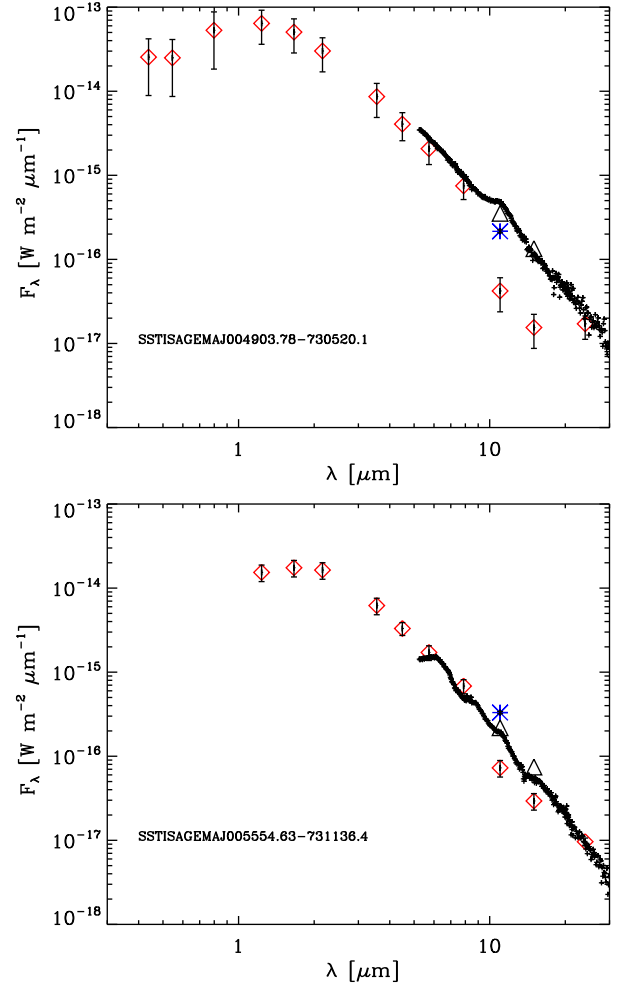


Figure A2. Two examples of sources showing the photometric data points taken from Srinivasan et al. (2016) (red diamonds) and from Ita et al. (2010) (blue asterisks). The *Akari* S11 and L15 fluxes, computed convolving the filters with the observed IRS spectra, are represented by black triangles. The IRS spectra are also plotted with black crosses.

Another star (J012606.02–720921.0) is instead characterized by an observed photometry that cannot be reproduced by a SED from an AGB star, as already concluded by the fitting procedure of Srinivasan et al. (2016).

We exclude from the fit the photometry at 24 μm for all the FIR sources, since by definition FIR sources are more luminous at 24 μm than at 8 μm and the 24 μm flux cannot be fitted by the SED of an AGB. The additional optical and NIR photometry excluded from the fitting procedure are listed in Table A1.

For one additional source photometrically classified as C-rich (J011032.12–714146.3), the photometry at 24 μm appears to be unrelated to the SED.

This paper has been typeset from a $\text{\TeX}/\text{\LaTeX}$ file prepared by the author.